

# Near-field plume-surface interaction and regolith erosion and dispersal during the lunar landing

A. Rahimi<sup>a</sup>, O. Ejtehad<sup>a,b</sup>, K. H. Lee<sup>c</sup>, R. S. Myong<sup>a,\*</sup>

<sup>a</sup> School of Mechanical and Aerospace Engineering, and ACTRC, Gyeongsang National University, Jinju, South Korea

<sup>b</sup> Supercomputing Modeling and Simulation Center, Korea Institute of Science and Technology Information (KISTI), Daejeon, South Korea

<sup>c</sup> Department of Aerospace Engineering, Sejong University, South Korea

## Abstract:

A rocket plume impinging on the lunar surface when a lunar lander approaches a landing site can cause significant dust dispersal. This study investigated the near-field rocket plume-lunar surface interaction and subsequent regolith erosion and particle dispersal. These subjects are challenging because of the complicated flow physics associated with the inherently multi-physics multi-scale problem, and the special lunar conditions, characterized by micro-gravity, near-vacuum, extreme dryness, and the unique properties of the regolith. Gas expansion into the near-vacuum lunar condition compared to exhaust gas under terrestrial circumstances varies not only in the shape of plume but also in the pressure profile on the surface. To understand the effect of surface erosion on flow characteristics, in conjunction with the finite volume method of plume impingement of a rocket nozzle, the Roberts erosion model was introduced for the influx mass flow rate of dust particles based on excess shear stress. The particulate phase was then handled in a Lagrangian framework using the discrete phase model. A parametric study on erosion rate was also conducted to examine the effect of particle density, particle diameter, Mach number, and hover altitude. Additionally, the maximum speed and inclined angle of the particles from the surface were computed for

---

\* Corresponding author.  
E-mail address: [myong@gnu.ac.kr](mailto:myong@gnu.ac.kr) (R.S. Myong).

various particle diameters and hover altitudes. The resulting information about the pressure and heat flux distribution on lunar module components can be used for engineering design. Finally, high-fidelity simulations of particles eroded from the surface indicated that several scenarios may occur depending on particle diameters, grain-inclined angles from the surface, and hover altitudes.

**Keywords:** Lunar landing, plume-surface interaction, surface erosion, discrete phase model

## 1. Introduction

Fifty years after Apollo 11's the first Moon landing [1], lunar exploration has recently been resumed. While early lunar exploration was largely propelled by national prestige, the driving force now is the pursuit of opportunities to expand the economic sphere of the Earth to the Moon. Such opportunities include, for example, the discovery of water ice in the craters of the south pole of the Moon [2].

Reaching the Moon involves several stages, including launching from the earth, Earth-Moon transfer, circumlunar orbit, and the final powered descent phase [3]. During the powered descent phase of landing on the Moon, as well as the ascent from the lunar surface after exploration, a knotty dusty gas problem may occur, caused by the rapid expansion of rocket motor gas through the nozzle and its subsequent interaction with the lunar surface.

When the lander approaches the lunar surface in the final step of the landing procedure, the plume flow may be deflected toward the lander and hit components loaded on the module. This deflected flow may exert disturbing torque as well as heat flux on sensitive parts of the lander. Further, once the rocket motor plume interacts with the lunar surface, some eroded particles from the regolith may be entrained into the flow field. These particles can not only alter the flow features, but can also damage module elements of the explorer or previously

settled vehicles and equipment at adjacent sites.

Moreover, as observed in the Apollo programs (11, 12, 14-17), the particles can block vision and cause the mal-functioning of tracking sensors. In fact, to minimize the effects of dust, the later Apollo 14 program adopted a pinpoint landing procedure, rather than the initial Apollo 11's landing procedure, which allowed the lander to move horizontally a considerable distance at low altitude while under the dust influence. Also, in NASA's 2012 Mars Science Laboratory mission with the Curiosity lander, a two-step soft landing was adopted. This involved, first, hovering at an altitude high enough to avoid dust effects, and second, lowering the rover down to the Mars surface on bridles and an umbilical cord (called the Sky Crane maneuver).

In addition, the entrained particles may jeopardize long-term exploration that relies on solar panels, which can be degraded by thermal effects and dust contamination. For these reasons, the Apollo astronaut John Young claimed "*Dust is the number one concern in returning to the Moon!*" [4]

A schematic of an impinging rocket motor plume and the subsequent dusty gas flow formed by the ejection of solid particles from the regolith is illustrated in Fig. 1. The multi-scale nature of the physical phenomena in this problem leads to the coexistence of various flow regimes; the plume expansion, shock and stagnation regions, local erosion, granular flow, dusty jet flow, and rarefied flow, which make the computational simulation extremely challenging [5].

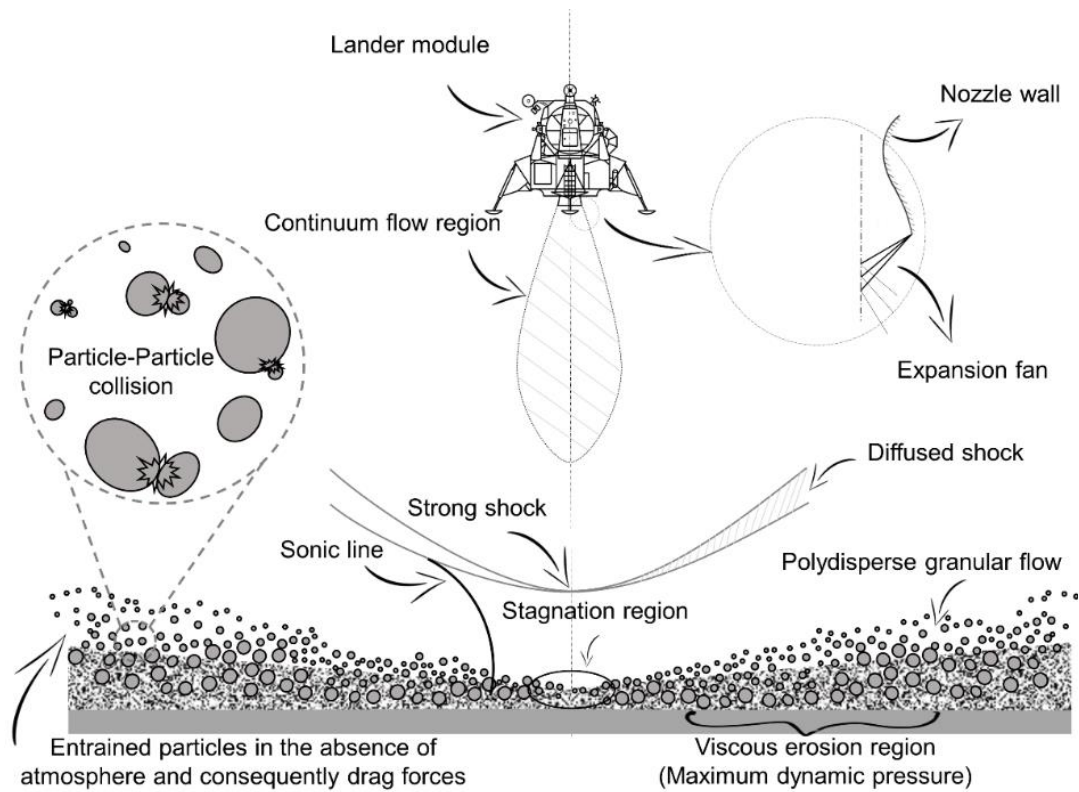


**Fig. 1.** Schematic of an impinging rocket motor plume and the subsequent dusty gas flow formed by the ejection of solid particles from the regolith during the lunar landing

In the last few decades, various studies have investigated not only the rocket nozzle plume [6, 7], but also the effect of exhaust gas on the field of operation [8-11], the lander module components in space missions [12], and the surface of the landing site. As demonstrated in [13], the erosion can be influenced by nozzle characteristics, including the thrust level, the hover altitude, and the degree of expansion of the jet, as well as regolith cohesion strength and particle size.

It must be noted that the experimental setup in which a rocket engine is fired into a dusty bed (with many unknown characteristics) while the vacuum condition and low gravity are maintained is a daunting task, if not impossible. This fact makes computational fluid dynamics (CFD) a valuable tool for the prediction of this type of flow regime. The conventional methods for simulating rarefied multiphase flows formed in the descent phase of the lunar lander are direct simulation Monte Carlo (DSMC) method or a hybrid (CFD-

DSMC) method [14, 15]. Analytical solution for the highly rarefied jet in the collision-less limit has been derived in the case of jet impingement on a flat surface [16]. Cai *et al.* [17, 18] investigated the effects of rarefaction on jet impingement loads for a variety of regimes from continuum to collision-less flows, and verified the results with DSMC solutions.

He *et al.* [19] illustrated the aerodynamic effects of cushion engines on the explorer's bottom, the landfall legs, and antenna in China "Tanyue" project. They conducted a simulation study based on the DSMC method to analyze the engine plume and its impacts on the lander components. It showed the existence of compression waves near the landfall legs, as well as high-pressure regions on the bottom caused by the presence of the landfall legs. In another work, Yim *et al.* [20] carried out an analysis for European service modules (ESM) on the plume effects of various engines, such as the reaction control system (RCS), auxiliary engines, and orbital maneuvering system engine (OMS-E). They evaluated the heat flux generated by the plume on sensitive surfaces, and particularly on the solar panels, during a thermal analysis of the ESM engine. Sharma *et al.* [21] investigated the effect of multiple engine plumes and thermal load on the India's second lunar exploration mission, Chandrayaan-2, using a Navier-Stokes solver coupled with the radiative transport equation. Zheng *et al.* [22] and Wei *et al.* [23] investigated the dynamics of soft-landing under different scenarios to guide the future design of manned lander or larger modules in lunar landing missions.

In the present study, we investigated the near-field rocket plume-lunar surface interaction and subsequent regolith erosion and particle dispersal in detail. As the first task for this endeavor, the physical conservation laws with the classical constitutive relations of Navier-Stokes-Fourier (NSF) were solved, based on a FVM discretization. It is well-known that the NSF equations will fail to predict the flow in a highly rarefied condition. Therefore, applying

the NSF model to problems in the near-vacuum condition of the Moon may be questionable.

However, when the focus is the near-field interaction of the plume and surface in a low altitude hover on the order of a few meters, most flow regimes turn out to be in either continuum or near-continuum. Further, for a five-nozzle configuration, the situation becomes even closer to the continuum condition. The use of the NSF model in the present problem will be justified by a comprehensive analysis of the degree of local thermal non-equilibrium in the dynamic flow field based on the non-equilibrium entropy production associated with the energy dissipation arising from molecular collisions. Therefore, the present methodology can be regarded as an efficient simulation tool for engineering design purposes, compared to the previous computationally expensive DSMC method. Nonetheless, the second-order Boltzmann-based constitutive relations developed by the authors [24-28] beyond the present first-order NSF constitutive relations may be necessary for a more accurate and far-field description of this challenging problem.

Another vital piece in the present work is the regolith erosion and particle dispersal, both of which demand challenging modeling work. Few numerical works have been devoted to the study of the existence of solid particles in the plume flow field and their interaction. The DSMC approach proposed by Gallis *et al.* [29] was extended by Burt and Boyd [30] for solving the transport of spherical particles in a rarefied gas flow via the two-way coupling. Moreover, few studies modeling the regolith erosion and the effect of entrained particles on the gaseous phase have been reported in the past. Mathematical modeling and simulation of erosion phenomena for plume impingement on the surface for the Apollo mission was pioneered by Roberts [31, 32]. Based on the density distribution at the nozzle exit and the gas properties on the surface derived by normal shock relations, he calculated pressure distribution on the surface in terms of hover altitude, nozzle Mach number, the ratio of

specific heats and pressure of the chamber. In another important work by Lane and Metzger [33], the trajectory of grains was predicted by utilizing the DSMC solution as an input for simple equations of the particle trajectory model (PTM). In addition, they modified the drag and lift equations to include the rarefaction and compressibility effects [34]. In another study, Li *et al.* [35] considered two-way coupling model of gas-particle flow with two different methods of treating particles to obtain better insight of the impact of entrained grains on the module and surrounding area.

To treat particle dispersal in gas, there are two distinctive approaches; Lagrangian and Eulerian [36]. In the present study, we employ a Lagrangian framework in which one- and two-way coupling of the discrete phase model (DPM) [37] with the NSF equations is easily described. In this model, particles are injected into the domain to simulate the eroded lunar surface particles. The coupling between the dust and gas can be either one or two-way, depending on the level of interaction of the phases. To determine the rate of particle influx, the Roberts model based on excess shear stress in [38] is applied at the lunar surface boundary. In addition, a sensitivity analysis on the effect of the variation of parameters on erosion influx in the Roberts model was conducted. Finally, the maximum speed and inclined angle of the particles from the surface were computed for various particle diameters and hover altitudes, which may provide valuable information for the analysis of landing procedures.

## **2. Computational models and numerical method**

### **2.1 Compressible Navier-Stokes-Fourier equations for the gas phase**

The computational domain is divided using a finite set of control volumes to approximate the conservation equations of mass, momentum, and energy, utilizing the finite volume

method (FVM). The FVM is a robust and efficient method for solving a hyperbolic system of equations [39]. The flux on a cell surface was determined by the advection upstream splitting method plus (AUSM+). The AUSM+ scheme shows functional capabilities for resolving discontinuities and providing entropy-satisfying and positivity-preserving solutions, after overcoming a deficiency related to oscillatory pressure observed along the grid direction for very small velocities in the early stage of its development [40]. The density-based approach in the ANSYS FLUENT (version 17.2) CFD code was employed. The viscosity for the ideal gas assumption was calculated using Sutherland's law to take into account the dependency on temperature.

## 2.2 Discrete phase model for dust phase

In the current study, the trajectory and the behavior of the scattered particles in the continuous phase are modeled in a Lagrangian framework using the discrete phase model (DPM) by integrating the force balance over each particle. In this model, the assumption of neglecting particle-particle interaction is valid, since the volume fraction of the dispersed phase compared to the continuous phase is significantly low (less than 10%). The DPM can be expressed in a way that makes simulation of the heat and momentum exchange feasible, by conducting two-way coupling with the Eulerian frame of gas. The force balance equation can be written in the  $x$ -direction for simplicity, as follows:

$$\frac{du_p}{dt} = F_D(u - u_p) + \frac{g_x(\rho_p - \rho)}{\rho_p} \quad (1)$$

In the above equation,  $F_D$  is the drag force per unit mass and can be expressed as

$$F_D = \frac{18\mu}{\rho_p d_p^2} \frac{C_D Re}{24} \quad (2)$$

Here  $u$ ,  $\rho$ ,  $\mu$  and  $d$ , are velocity, density, viscosity, and diameter, respectively. The subscript  $p$  represents the property of particle.  $g$  is the gravitational acceleration and  $Re$  is the relative Reynolds number defined as

$$Re = \frac{\rho d_p |u - u_p|}{\mu} \quad (3)$$

where the drag coefficient  $C_D$  is given by

$$C_D = a_1 + \frac{a_2}{Re} + \frac{a_3}{Re^2} \quad (4)$$

Here  $a_1$ ,  $a_2$  and  $a_3$  represent constant coefficients for smooth spherical particles [41, 42]. The above expression approximates the drag coefficient based on the standard experimental drag-Reynolds-number relationship for spherical shape of particles, which covers a wide range of flow with various Reynolds numbers [43].

### 3. Erosion mechanisms and mathematical modeling

Surface erosion refers to the process of solid particles being lifted from the lunar regolith surface by the rocket motor plume gas. The rate of this process is known as the erosion rate. Four different mechanisms have been identified for this erosion by Metzger *et al.* [44] as follows:

**Diffusion-driven flow (DDF):** The drag force of a gas jet through the pore spaces of the soil reacts against the grains generating a distributed body force in the bulk of the soil which can shear the material.

**Diffused gas eruption (DGE):** Diffused gas eruption occurs when the gas penetrates a porous media and loosens the porous soil, such that the soil layer is fluidized.

**Bearing capacity failure (BCF):** When the pressure becomes higher than the bearing capacity of the soil, a narrow cup shape is created which has unstable circumstances and can easily collapse under the gravity force.

**Viscous erosion (VE):** Viscous erosion takes place when the shear stress on the surface overcomes the critical cohesive strength of the soil and causes the solid particles to creep along the surface. The rolled particles elevate the possibility of particle-particle collision; accordingly, these collisions by themselves can lead to scattering of the particles into the flow field.

The dominant erosion mechanism on the lunar surface is viscous erosion, due to the existence of a vacuum: the soil layers are tightly packed such that the gas cannot drive into the lunar soil bed. In contrast, the BCF mechanism is negligible because of the high packing density and bearing capacity of the lunar regolith. The VE mechanism can be classified as 1) aerodynamic entrainment, in which aerodynamic forces are dominant compared to gravitational forces; 2) saltation bombardment, in which high-energy particles dislodge other particles by colliding, and 3) aggregate disintegration, when particles bound together by thermal cycling and cohesion break apart when they are impacted by a significant force [45]. The aforementioned erosion mechanisms and their respective importance in the lunar landing problem are summarized in Fig. 2.

In the present study, the Roberts erosion model [38] of viscous erosion associated with aerodynamic entrainment is used to account for regolith erosion on the lunar surface. When the induced shear stress on the surface exceeds the threshold stress, erosion with a mass flux proportional to the excess shear will occur:

$$\frac{1}{2} au \phi = \tau - \tau_c \quad (5)$$

In the above equation,  $\phi$  is the erosion rate (mass flux),  $a$  is the fraction velocity that the particles gain from the carrier phase,  $u$  is the gas phase velocity,  $\tau$  is the shear stress on the surface, and  $\tau_{crit}$  is the threshold stress, which can be defined as:

$$\tau_{crit} = C + P \tan \varphi \quad (6)$$

Here,  $C$ ,  $P$ , and  $\varphi$  are cohesive stress, gas static pressure on surface, and friction angle, respectively. The coefficient  $a$  in the fraction velocity can be expressed as follows:

$$a = \left[ \frac{1}{2} + \sqrt{\frac{1}{4} + \frac{1}{\zeta}} \right]^{-1} \quad (7)$$

$$\zeta = \frac{18\mu_c h}{\rho_p \sqrt{RT_c} (4 + k_h)} \left[ \frac{1}{d_p^2} + \frac{1}{d_p} \frac{(4 + k_h) C_D F_{th}}{72 \exp(1) \sqrt{2RT_c} \mu_c} \right] \quad (8)$$

As indicated in equations (7) and (8), the coefficient  $a$  is dependent on various parameters. In equation (8),  $\mu_c$  and  $T_c$  are the engine chamber viscosity and temperature, respectively.  $h$ ,  $\rho_p$  and  $d_p$  are the hover altitude, particle density, and particle diameter of the regolith, respectively. The  $k_h$  is the hypersonic factor defined by  $\gamma(\gamma - 1)M_n^2$ , where  $\gamma$  and  $M_n$  are the ratio of specific heats and the Mach number at the nozzle exit plane. In addition,  $\zeta$  is related to gas constant  $R$ , as well as drag coefficient  $C_D$  (assumed 0.2 by Roberts) and engine thrust  $F_{th}$ .

As can be seen in equations (7) and (8), the fraction of particle velocity is a function of several parameters which may influence the erosion mass flux. Furthermore, there is no comprehensive information regarding the Roberts erosion model in the literature. For these reasons, a sensitivity analysis may be helpful to gain insight into its sensible use before actual simulation, which will be described in Section 5.2.

To simulate the eroded particles that are injected into the flow field, the DPM module was used. The erosion mass flux as a function of axial direction was calculated by implementing an erosion model via the user defined function (UDF) feature of the FLUENT code. To compute the mass flow rate of injected particles via equation (5), the shear stress on the regolith surface needs to be estimated.

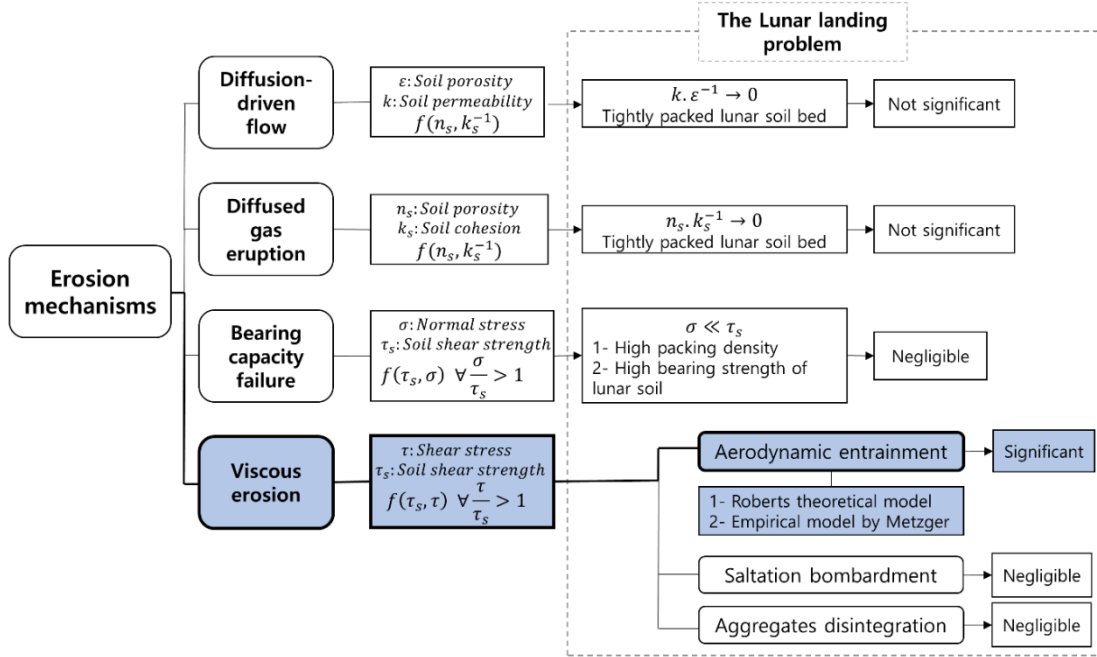


Fig. 2. Erosion mechanisms and their respective importance in the lunar landing problem

#### 4. Verification and validation of the numerical method

##### 4.1 Benchmark problem for verification of the carrier gas phase

Due to the lack of experimental results for the proposed lunar lander, the Apollo 11 nozzle was considered to verify the numerical simulation. The internal flow inside the nozzle was simulated by assuming the working gas to be a polyatomic water vapor (which is a good representation of the actual exhaust gas), and the solutions at the nozzle exit were compared with the results of the DPLR code developed at the NASA Ames research center [46]. As shown in Fig. 3, the velocity, density, and temperature profiles were found to be in good

qualitative agreement, except for some deviations in temperature due to the different types of gas.

The impingement of the rocket motor plume on the lunar surface in a hovering altitude of 5m was also investigated. Surprisingly, the solutions of the current work (NSF) were found to be in good agreement with the DSMC solutions of Morris [46], including pressure contours as low as 20 Pa, as depicted in Fig. 4. An internal shock, formed inside the nozzle, is reflected from the axis of symmetry and interacts with the stand-off shock near the lunar surface. These discontinuities are well resolved by the present CFD method and the hybrid CFD-DSMC method [46] in which the gas flow near the nozzle is solved by a CFD approach.

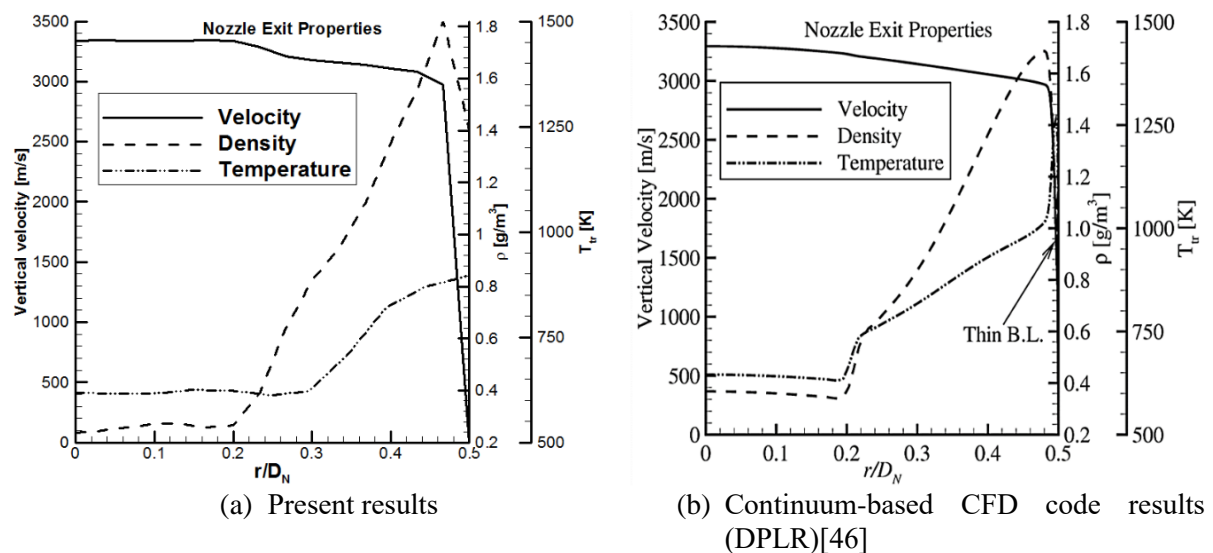


**Fig. 3.** Verification of numerical solutions for the gas phase at the nozzle exit

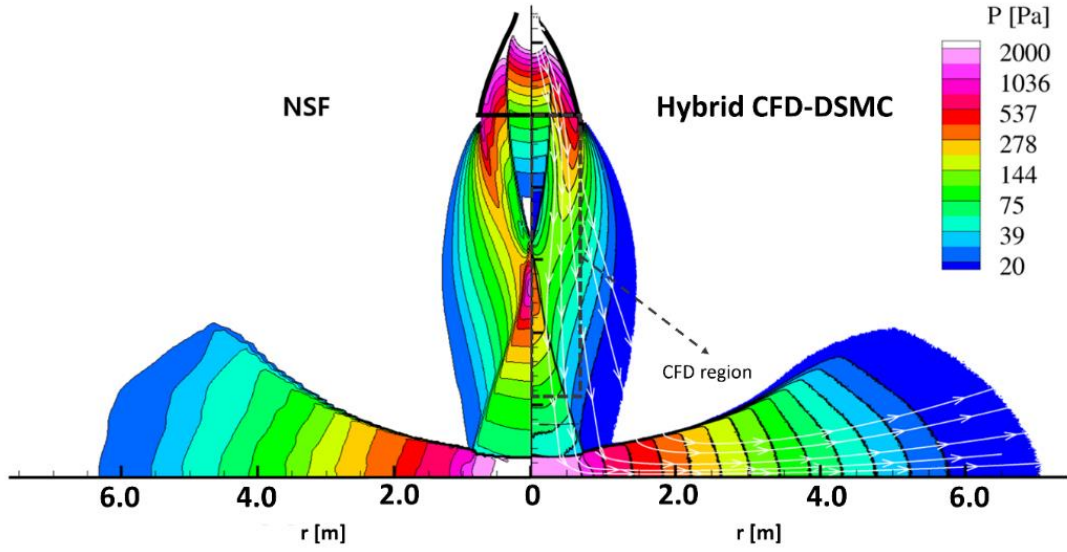


**Fig. 4.** Verification of numerical solutions (pressure): present work (left); DSMC [46] (right)

In order to elaborate on the validity of the present findings, a non-equilibrium quantifier based on a combination of the Knudsen ( $Kn$ ) and Mach ( $M$ ) numbers was introduced to evaluate the degree of deviation that might be present in the first-order NSF constitutive laws. As noted first by Tsien in 1946 [47, 48] ‘the order of magnitude of the additional second-order heat flux or stresses is  $Kn \cdot M$ ,’ rather than  $Kn$  alone, and therefore the degree of non-equilibrium in the moving gases should be the ratio of the viscous force to the pressure, since the viscous force is a direct consequence of the thermal non-equilibrium [47, 48]. In this context, it should be mentioned that the Knudsen number is a pure thermodynamic quantity without any reference to the average velocity of gas molecules. A non-equilibrium quantifier to incorporate the average velocity of gas molecules,  $N_\delta$ , is then expressed as  $N_\delta = KnM(2\gamma/\pi)^{0.5}$ . Since the quantifier  $N_\delta$  in the *moving* gases represents the relative magnitude of off-diagonal terms in the second-order rank tensor of the stress, the value  $N_\delta = 1.0$  means that the magnitude of the off-diagonal terms (viscous stress) is comparable to the diagonal term (hydrostatic pressure), implying a high degree of non-equilibrium.

The contours of the local non-equilibrium quantifier in a dynamic flow field are plotted

along with the local Knudsen and Mach numbers in Fig. 5(a)-(c). Seven representative locations in the computational domain are marked with numbers to classify flow regimes according to the degree of non-equilibrium depicted in Fig. 5(d). Among the marks shown in Fig. 5(d), regions 1 to 3 fall very close to the equilibrium regime, and region 4 belongs to a state near equilibrium. Regions 5 and 6 belong to a state slightly deviated from equilibrium, while region 7 belongs to a regime considerably deviated from equilibrium.

However, none of these regions approach a highly non-equilibrium state, since  $N_\delta$  values rarely exceed 0.1, as shown in Fig. 5(c), (d). Moreover, due to the presence of the lunar surface in front of the gas expansion, even these maximum non-equilibrium states are formed only in very narrow region 7 and in regions far from standoff shocks, making most of the near-field regions near- or slightly deviated from equilibrium. This observation explains the physical reason behind the good agreement of the NSF solutions with the DSMC solutions in the present flow problem.

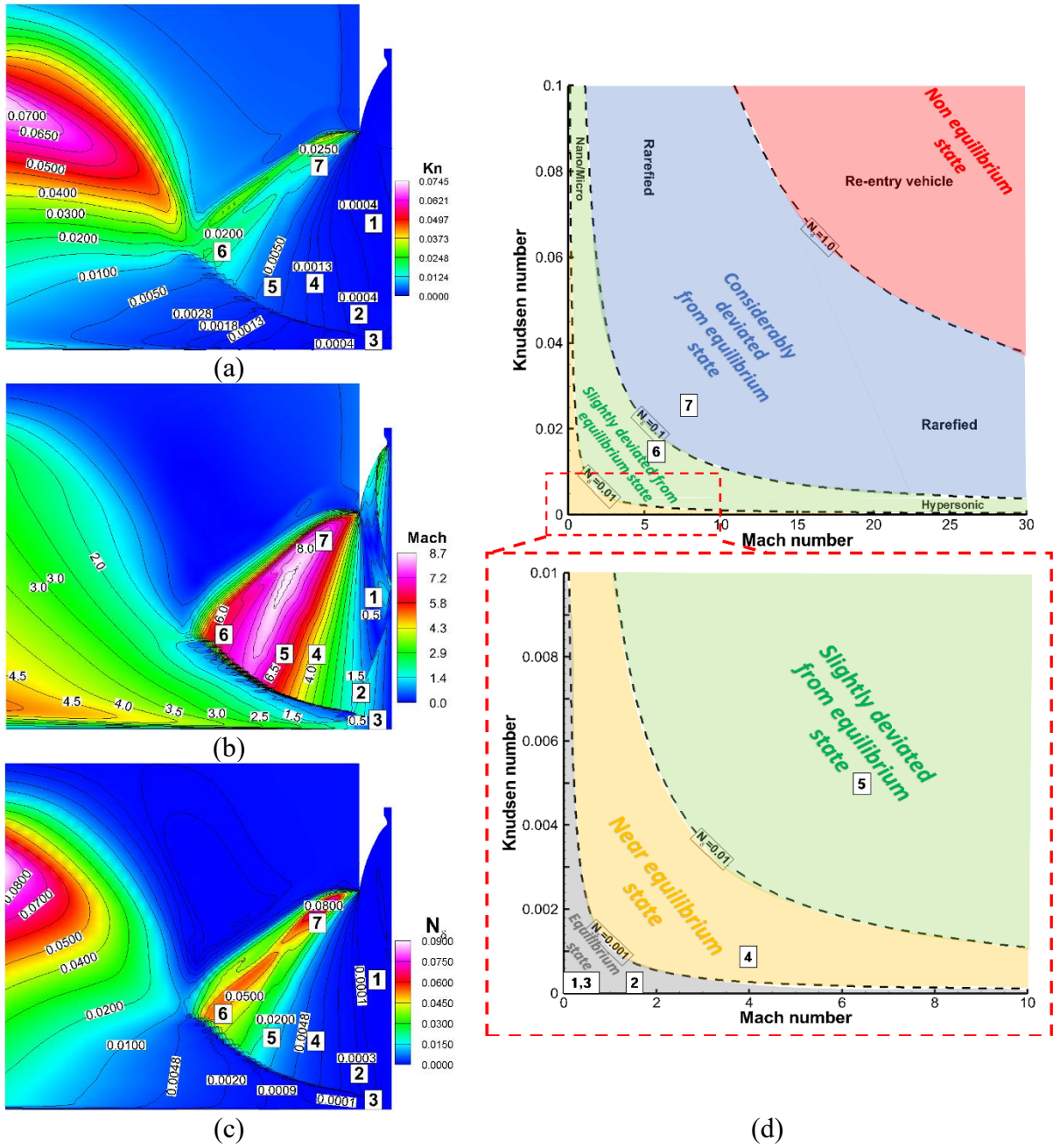


**Fig. 5.** Flow classification based on  $Kn$ ,  $M$  and  $N_\delta$  for the Apollo nozzle flow problem

#### 4.2 Benchmark problem for the validation of gas-particle interaction

In order to check the fidelity of the Eulerian-Lagrangian approach, the under-expanded supersonic jets of gas and particle—one of the few cases where experimental studies were reported on the interaction of particles with shock waves—is considered. The problem is defined as a supersonic jet which is expanded from a high-pressure chamber into a low-

pressure chamber, along with injected particles from nozzle. A comparison of dusty gas solutions with experimental data [49] in Mach disc location is illustrated in Table 1. In this flow, one of the critical features is the upstream movement of the Mach disc as a consequence of the interaction of gas phase with particles. As it was reported in [49], when the particle loading increases, the Mach disc gets closer to the nozzle exit and the wave patterns in the downstream of the Mach disc become more pronounced. The comparison reveals that the present approach adequately predicts the movement of the Mach disc.

**Table 1** Comparison of numerical and experimental results for Mach disc location at various particulate loading ( $p_0 = 0.306 \text{ MPa}$ ,  $p_0 / p_\infty = 29.8$ ,  $D_p = 26 \mu\text{m}$ )

| Mach disc location<br>Particulate loading | $X_m/D$<br>Experimental results<br>[49] | $X_m/D$<br>Eulerian-Lagrangian<br>numerical simulation |
|---|---|--|
| 0.0                                       | 3.8                                     | 3.77   |
| 0.26                                      | 3.54                                    | 3.6  |
| 0.38                                      | 3.15                                    | 3.2  |
| 0.66                                      | 2.8                                     | 3.1  |
| 1.08                                      | 2.5                                     | 2.8  |

## 5. Results and discussion: plume impingement, regolith erosion, and particle dispersal

### 5.1 Nozzle plume impingement on the lunar surface

Before investigating the complicated multiple nozzle/plume flow field, a single equivalent nozzle with the same mass flow rate and thrust was considered. The on-design operating condition of the descent engine of the proposed lunar lander was considered to study the near-field plume-surface interaction. The nozzle throat and exit diameters were 11.35 mm and 80.26 mm, respectively. The lander was assumed to hover at an altitude of 1m in all simulations. The axisymmetric boundary condition was applied to the nozzle axis to take 3D effects into account. Due to the geometrical symmetry of the nozzle, only half of the domain was solved. The computational domain assumed 60 and 30 times the nozzle exit diameter in

the axial and radial directions, respectively. The working gas was assumed to be a polyatomic water vapor (which is a good representation of the actual exhaust gas). The boundary conditions and prescribed values are summarized in Table 2.

**Table 2.** Boundary conditions in the axisymmetric simulation

|                 |                     |                |
|-----------------|---------------------|----------------|
| Pressure inlet  | Chamber pressure    | 1378.946 (kPa) |
|                 | Chamber temperature | 876.33 (K)     |
| Pressure outlet | Ambient pressure    | 5 (Pa)         |

As illustrated in Fig. 6, the gas flow emanates from the nozzle exit and expands into the low-pressure region, forming an under-expanded jet plume along with slip lines which maintain the pressure constant across the jet boundary [50]. The incident expansion waves after reflecting from the free boundary convert to compression waves and later form a shock wave.

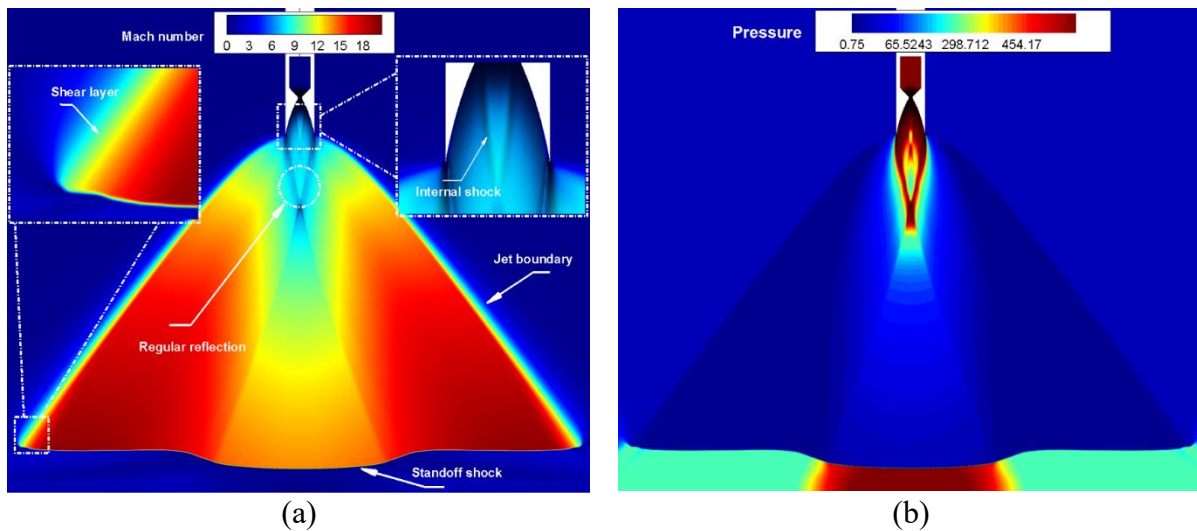


**Fig. 6.** Solutions of axisymmetric nozzle plume and surface interaction: a) Mach number, b) pressure

When the plume impinges on the surface, a stand-off bowl-shaped shock is formed which turns the flow radially outward. Moreover, the flow stagnates exactly underneath the nozzle axis so that the stagnation condition with maximum pressure is found at the intersection point of the nozzle axis and the surface. As the radial distance from the stagnation point increases,

the static pressure on the surface decreases. The bowl-shaped shock and the impingement surface resemble a diverging nozzle in which the flow is accelerated from zero velocity at the stagnation point to supersonic velocities while the density continually decreases.

As noted in [51], the jet expansion ratio, the ratio of nozzle exit pressure to ambient pressure, plays an essential role in determining both the structure of waves of plume and the angle of the jet expansion with respect to the centerline. The magnitude of this parameter under the Earth circumstances is less than one. On the other hand, the parameter increases when the jet is exhausted into low-pressure lunar condition, forming the underexpanded jet. The effects of the different jet expansion ratio resulting from the pressure difference in lunar and terrestrial conditions can be observed in ground pressure profiles. Therefore, the accurate prediction of jet expansion ratio will be critical for a rigorous assessment of plume-surface interaction in terms of propulsion system requirements during the lunar landing.

As was done for the Apollo nozzle case, seven representative locations in the computational domain, marked with numbers in Fig. 7, were considered to evaluate the degree of non-equilibrium in the moving gases. As shown in Fig. 7(a) illustration of the degree of non-equilibrium, region 5 falls very close to the equilibrium regime, and regions 1, 2, 3, 6, 7 belong to a state slightly deviated from equilibrium. On the other hand, region 4 inside a triangle defined by the jet boundary, the central weak wave, and the standoff shock belongs to a regime considerably deviated from equilibrium. Nonetheless, the regime with the maximum  $N_\delta$  value 0.33 ( $\ll 1.0$ ) may be still considered within the NSF framework.

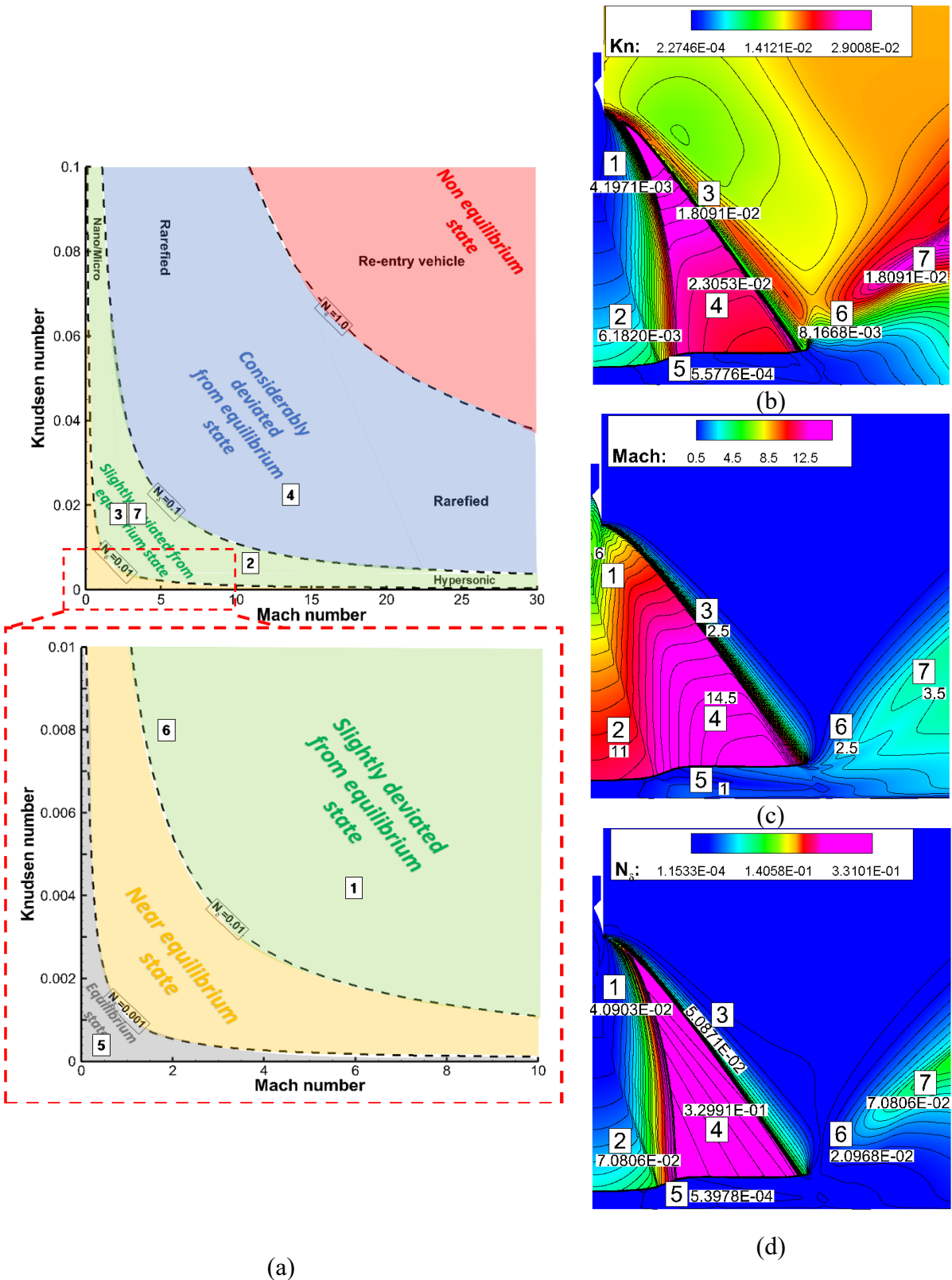


**Fig. 7.** Flow classification based on  $Kn$ ,  $M$  and  $N_\delta$  for a single nozzle jet case

As the next step, the complicated plume flow-field of multiple (five) nozzles was

investigated. Due to the symmetric geometry of the five-nozzle configuration, a quarter of the physical domain was simulated, as depicted in Fig. 8. In this three-dimensional simulation, not only the plume-surface/plume-plume interaction but also pressure distribution and thermal influences on the components of the lunar lander, including legs, were investigated.

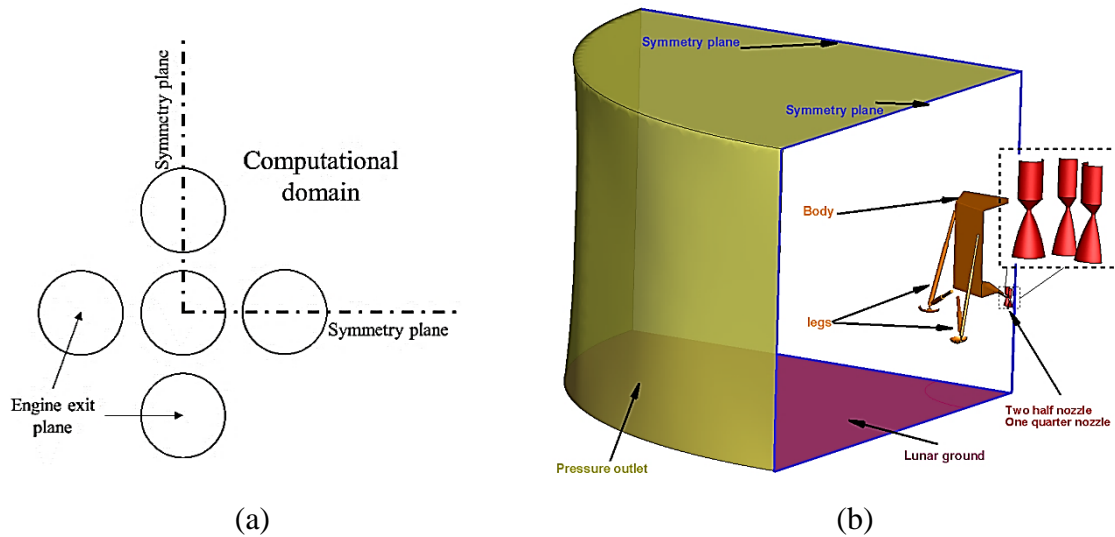


**Fig. 8.** Schematic of the computational domain for the five-nozzle configuration and symmetry planes

To obtain a better understanding of the plume-plume interactions, the Mach number and pressure on two cross-sections A and B (one along the three aligned engines and the other one rotated  $45^\circ$  compared to the first one) are plotted in Fig. 9. In Fig. 9(a), (c), (e), the Mach number contours on these cross-sections besides the 3D Mach iso-surface for certain Mach numbers are plotted. As can be seen, the Mach number is higher in section A-A compared to section B-B, due to interactions with the landfall legs which also lead to alteration of the plume shape—hindering the gas propagation. Similarly, Fig. 9(b), (d), (f) shows the pressure contours on two cross-sections besides the 3D pressure iso-surface.

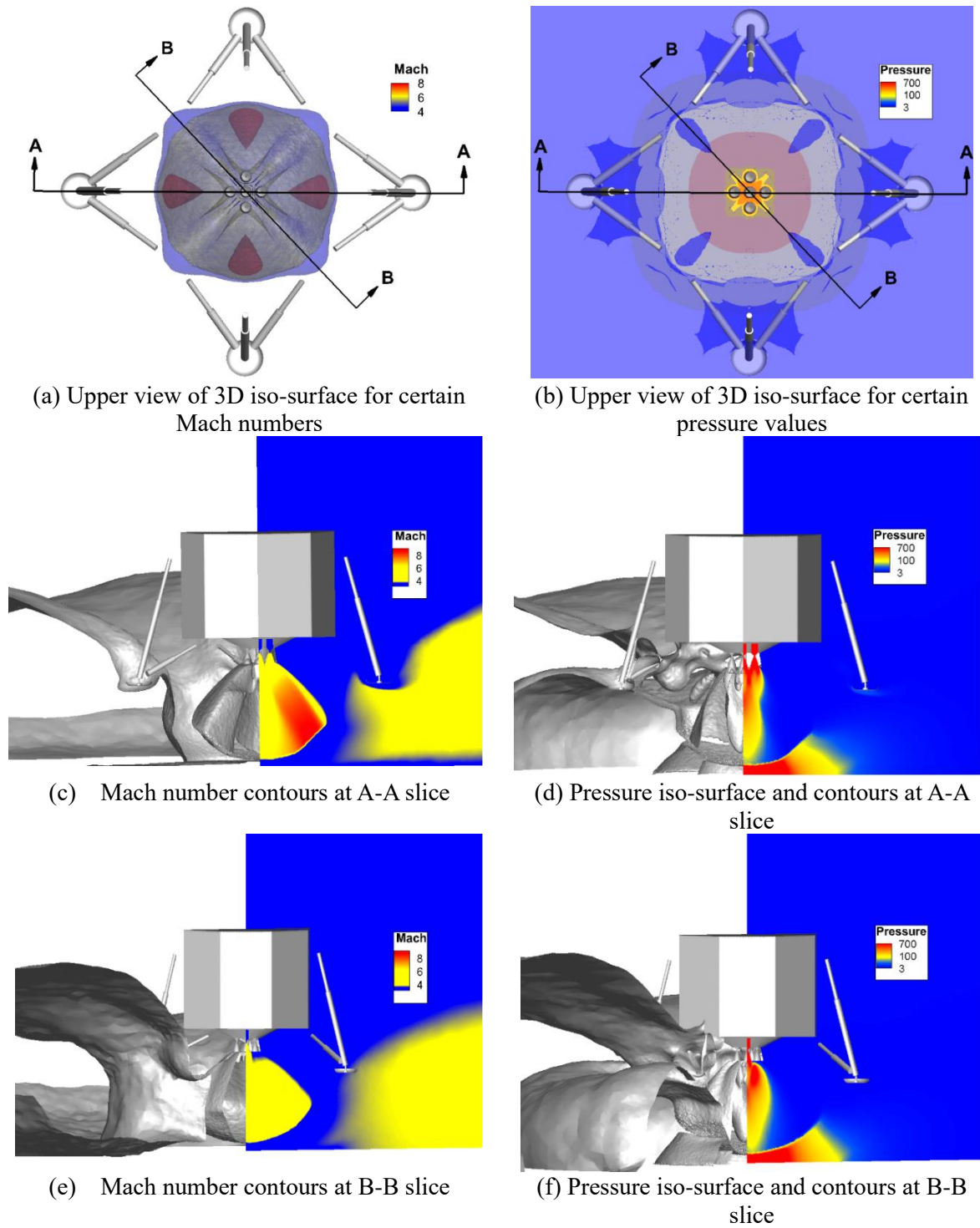


**Fig. 9.** 3D solutions of local Mach number and pressure

Mach number and temperature contours are also illustrated in Fig. 10. The essential features of the under-expanded jet impingement on a surface, including exhaust gas expansion, jet boundary, regular shock reflection, and standoff shock, are visible. For further

illustration, two cross-sections were selected, A-A, slightly below the nozzle exit, and B-B, moderately above the standoff shock. As shown in the A-A section, a regular shock reflection exists downstream of the nozzle exit. In contrast, the reflected shock has been eliminated in the B-B section. Compared to the axisymmetric engine (single nozzle engine), the plume expands further into the ambient region. Interestingly, no significant change in shock standoff distance was observed. Owing to strong plume-plume interaction, the Mach number for the five-engine configuration is significantly lower compared to the equivalent single nozzle case. Fig. 10(b) shows a substantial temperature increase—approximately one-third of the chamber's initial temperature—right after the shock reflection region.

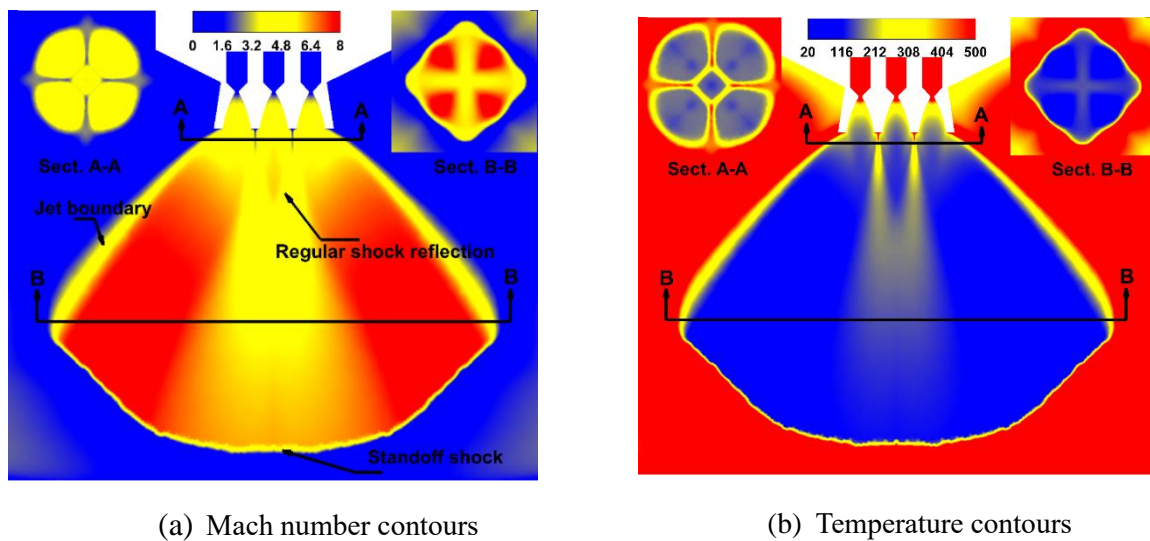
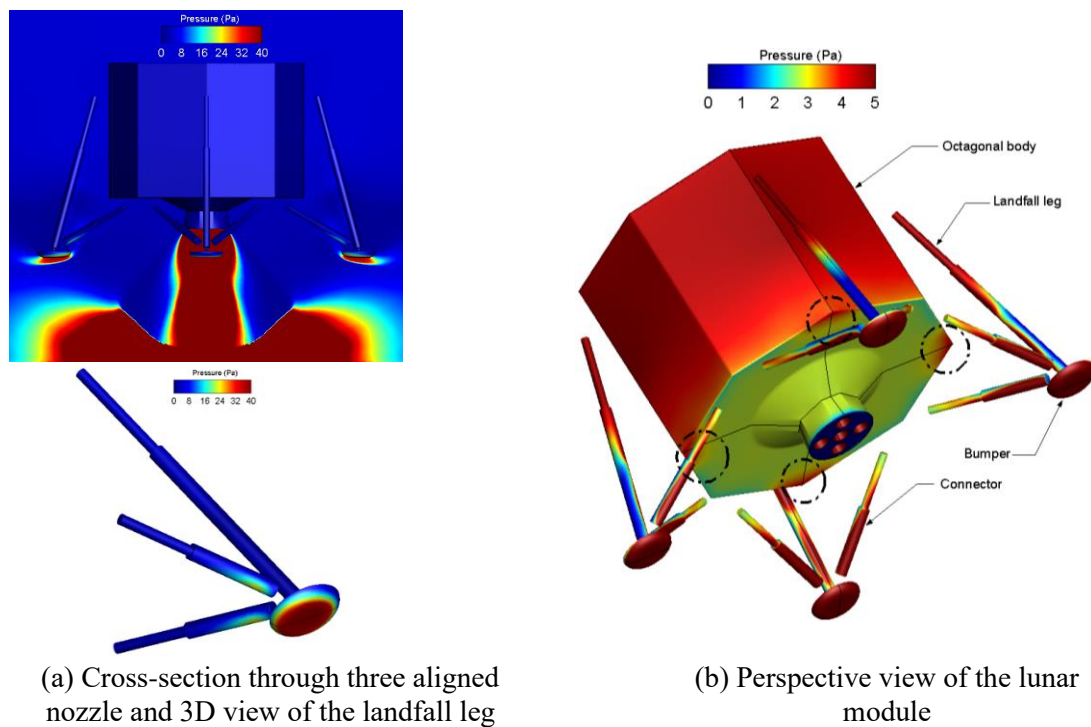


**Fig. 10.** Mach number and temperature contours on a cross-section along three aligned nozzles in the five-nozzle configuration

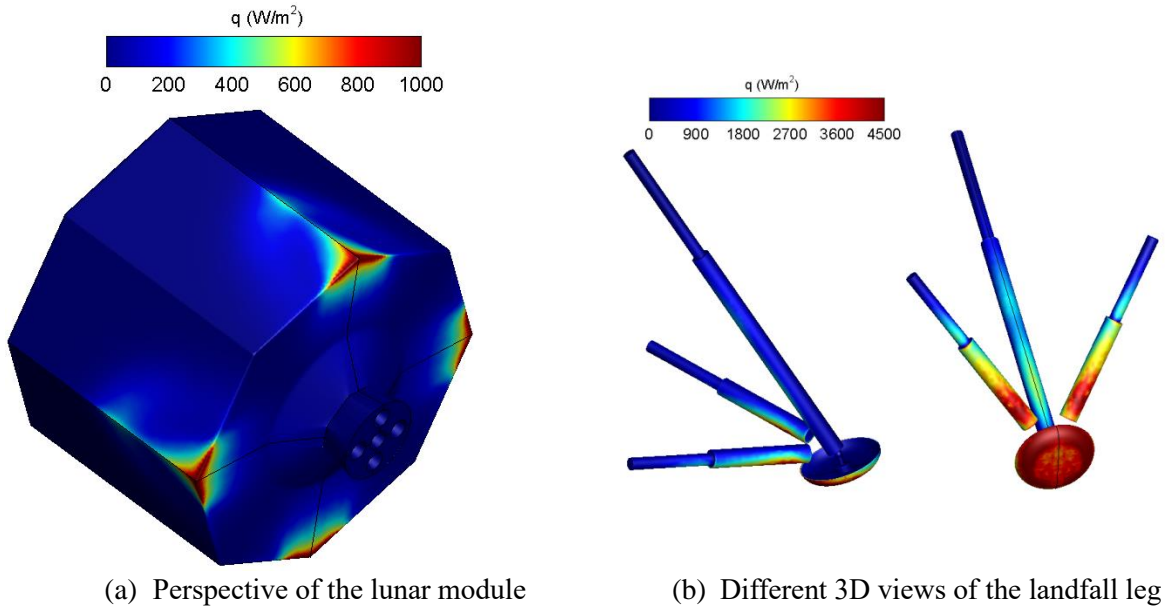
In the current work, it was possible to estimate the thermal influences and the effects of the aerodynamic force on the module components. Such analysis may have an essential role in the proper design of the lander configuration and the selection of materials for module components. The configuration of the proposed lunar lander consists of an octagonal body, four bumpers, four landfall legs, and eight connectors.

Fig. 11 shows the pressure contours on a cross-section passing the three aligned nozzles and

on the body surface of the explorer. From Fig. 11(a), three spots can be identified as a stagnation point; one at the intersection of the nozzle axis and the lunar surface, and the other two at the bottom of the landfall legs. At these points, the static pressure is much higher than the surrounding region. Moreover, the landfall legs create an obstacle and result in higher pressure distribution on the bottom surface of the bumper. The lower surface of the bumper connectors also experiences higher pressure, since it is directly exposed to the reflected gas flow from the lunar surface. The bottom of the module at four regions, marked by dash-dot circles, also experienced higher pressure compared to other areas on the explorer body, due to the presence of the four landfall legs, as shown in Fig. 11(b).



**Fig. 11.** Pressure distribution on lunar lander components



**Fig. 12.** Heat flux distribution on lunar lander module components

The reflected gas plume from the lunar surface causes not only high pressure on exposed surfaces but also high temperature through convection. As shown in Fig. 12, the heat flux distribution follows a trend similar to that of the pressure distribution. The maximum heat flux was observed on the four corners of the hexagonal body that face the bumpers.

The significant effect of plume-plume interaction in multi-nozzle configuration compared to a single nozzle can be seen in Figs. 13. Regions 1, 2, 3, 4, and 7 on the A-A slice fall very close to the equilibrium regime, and region 8 belongs to a near-equilibrium state. On the other hand, regions 5 and 6 belong to a state slightly deviated from equilibrium. Nonetheless, most of the regions near the nozzles are either in equilibrium or near equilibrium. In fact, the maximum  $N_\delta$  value 0.06 in Fig. 13(d) is far smaller than the  $N_\delta$  value 0.33 in Fig. 7(d) of the single nozzle case, implying multi-nozzle configuration leads to a reduction in the degree of non-equilibrium.

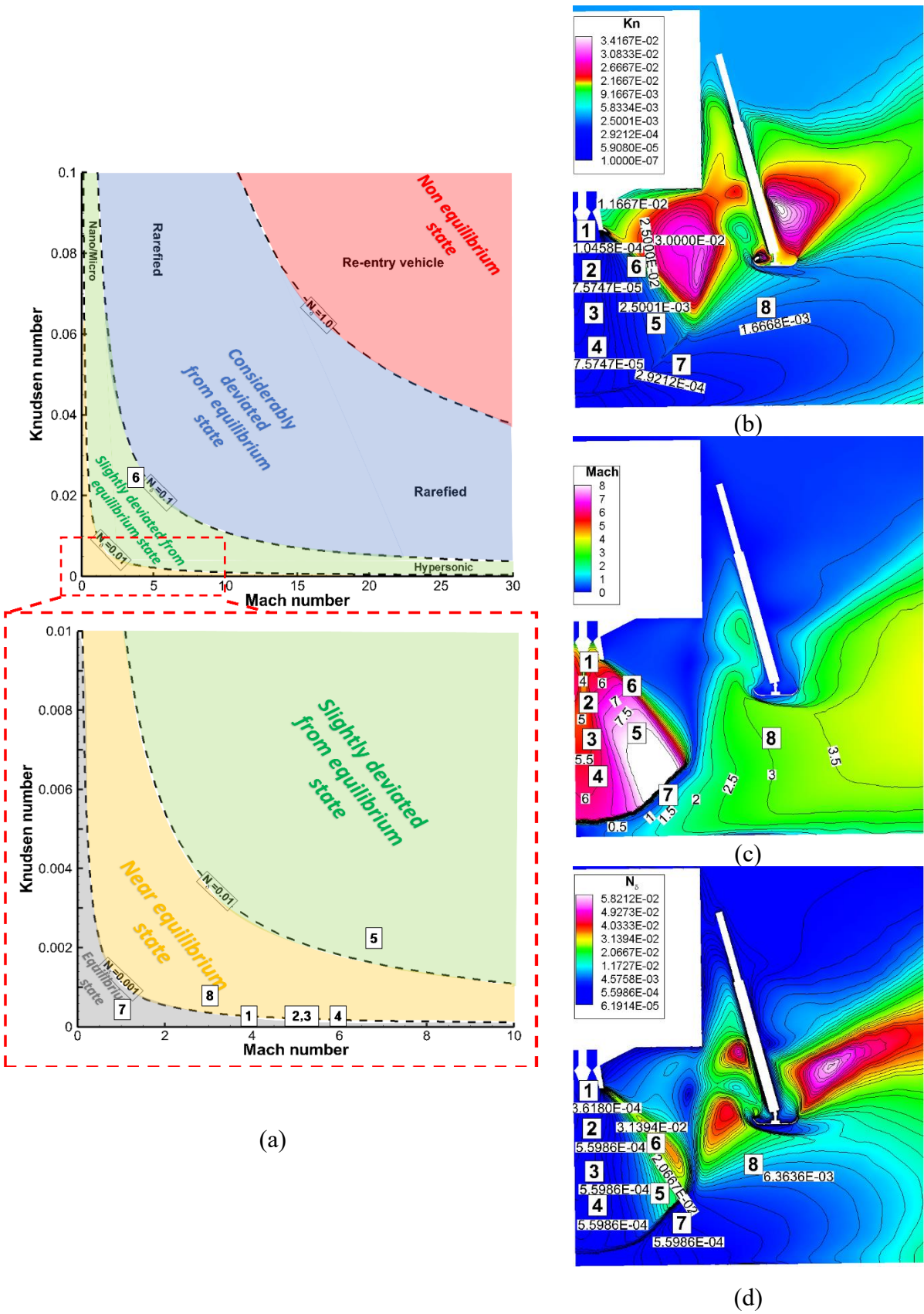


Fig. 13. Flow classification based on  $Kn$ ,  $M$  and  $N_\delta$  for five nozzles in operation at A-A slice

At this stage, it may be instructive to investigate the degree of non-equilibrium in the dynamic flow field in more detail, in particular, based on a non-equilibrium measure derived from the Rayleigh-Onsager dissipation function. Until now, the local  $N_\delta$ ,  $M$ , and Kn numbers have been computed to estimate the degree of non-equilibrium. The analysis based on these numbers revealed that most of the flow fields in the Apollo and five-nozzle configurations are either in equilibrium or near equilibrium. This observation can be justified in the case of a *low hover altitude with increasing ground effect and plume-plume interaction*. In the case of low hover altitude, the plume-surface interaction generates a strong standing shock near the lunar surface, and the initial high-speed flow from the nozzle is highly compressed along the core of the plume and is further decelerated to zero velocity at the stagnation point. As a result, the near-field flows are dominated by low speed (low  $M$ ) near the surface and high pressure (low Kn) in the core of the plume, forming flow-fields in continuum or near continuum. In the case of plume-plume interactions, because of momentum and energy exchange, the velocity and temperature are accordingly substantially decreased, and the local  $N_\delta$ ,  $M$ , and Kn numbers become much lower than the single-nozzle configuration, and a wider area of the flow field is in near equilibrium.

Nonetheless, there is still room to refine the present analysis of the degree of non-equilibrium in the moving gases. It should be noted that the effect of heat flux is completely omitted in the local  $N_\delta$ ,  $M$ , and Kn numbers, though heat flux will definitely play a physical role in thermal non-equilibrium. A better non-equilibrium measure can thus be derived based on the Rayleigh-Onsager dissipation function, which is a vital component in the theory of irreversible thermodynamics and is directly related to entropy production in non-equilibrium processes. A measure based on the energy dissipation arising from molecular collisions was introduced in [28] and can be expressed as follows:

$$\hat{R}^2 = \hat{\Pi} : \hat{\Pi} + \hat{\mathbf{Q}} \cdot \hat{\mathbf{Q}}, \quad (9)$$

$$\text{where } \hat{\Pi} \equiv \frac{N_\delta}{p} \mathbf{\Pi}, \quad \hat{\mathbf{Q}} \equiv \frac{N_\delta}{p} \frac{\mathbf{Q}}{\sqrt{T/(2\varepsilon)}}, \quad \varepsilon = \frac{1}{Ec} \frac{1}{Pr} \frac{1}{T_r / \Delta T}, \quad Ec = (\gamma - 1) M^2 (T_r / \Delta T).$$

Note that the measure  $\hat{R}$  is basically a combination of the global parameters  $N_\delta$ ,  $\varepsilon$ , and the local conserved properties  $p$ ,  $T$ , and the local non-conserved viscous shear stress  $\mathbf{\Pi}$  and heat flux  $\mathbf{Q}$ . And the second term in (9), a combination of  $\varepsilon$ ,  $T$  and  $\mathbf{Q}$ , represents the thermal and heat flux effects in the entropy production in non-equilibrium processes, overcoming the limitation of the simple measure  $N_\delta$ .

Fig. 14 shows the local non-equilibrium measure  $\hat{R}$  in regions where the flow experiences sudden changes and the degree of non-equilibrium is higher than other parts of the computational domain. Moreover, a comparison of Fig. 14(a) (the Apollo lander nozzle) and Fig. 14(b) (the proposed lunar lander nozzle) reveals that a more substantial portion of the domain is considerably deviated from equilibrium in the proposed lunar lander case. In fact, the non-equilibrium measure  $\hat{R}$  is approximately ten times higher than the Apollo lander case in almost every region of the domain.

On the other hand, a comparison of Fig. 14(b) (the single nozzle configuration) and Fig. 14(c) (the five-nozzle configuration) indicates that a greater portion of the domain in the five-nozzle configuration is either in equilibrium or near equilibrium. Therefore, based on the present in-depth analysis, it can be said that even the first-order constitutive relationships, namely the NSF equations, in conjunction with the physical conservation laws, can provide a fairly reasonable prediction of the near-field interaction of the plume (in particular, multiple plumes) and the lunar surface in meter-scale low altitude hover.

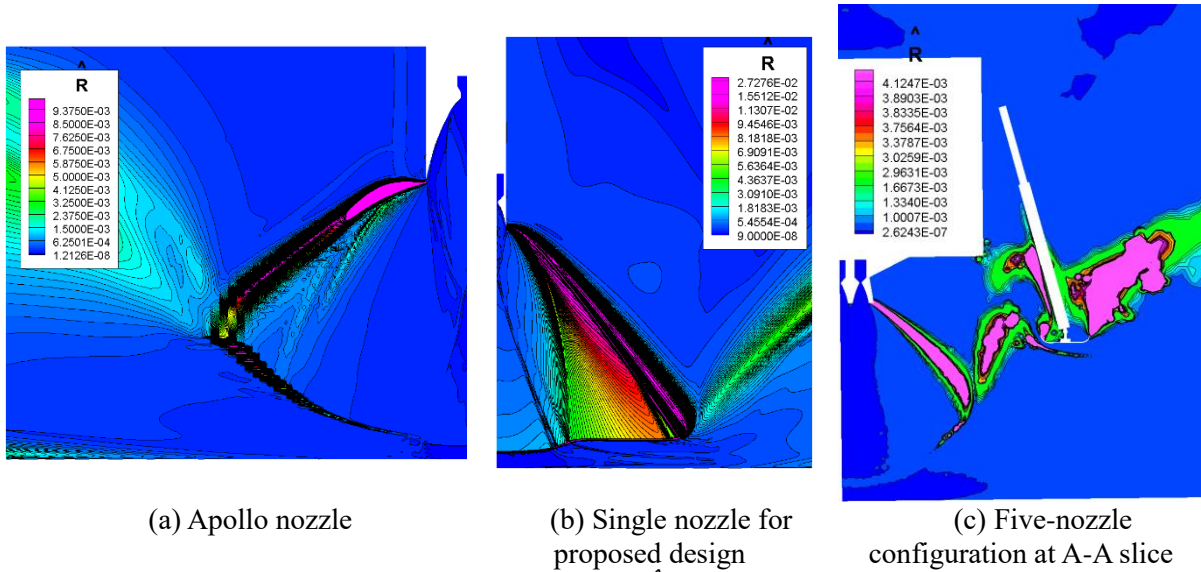


**Fig. 14.** Distribution of the non-equilibrium measure  $\hat{R}$  based on the entropy production for different nozzles

## 5.2 Simulation of erosion on the lunar surface

Another complexity arises in the surface erosion and dispersion of dust particles into the flowfield, which occur in wall jet near the surface induced by flow expansion. The entrained particles owing to gas-particle interaction may significantly alter the structure of the flow field. The presence of dust particles in gas flows with shocks and other discontinuities can give rise to peculiar phenomena; for instance, the formation of compound waves and Mach disc location displacement [36, 52]. Therefore, special attention should be paid to the critical effects of the particle's properties on structure of the flow-field, when analyzing the simulation results in such problems. In the present problem, the gas-particle collision in wall jet region resembles the dusty-gas underexpanded jet, since it comprises expansion waves and particle-laden region.

To simulate the surface erosion phenomena and the consequent entrainment of regolith grains, particles were injected from the surface based on the eroded mass flux via DPM. The present simulation methodology was first verified by using the DSMC solution for ammonia gas of Morris *et al.* [53]. An axisymmetric jet with uniform properties impinging on a dusty

surface was simulated. A constant wall temperature of 1000K was imposed on the lunar surface. A schematic of the problem and boundary conditions is illustrated in Fig. 15(a).

The cohesive stress and the friction angle were assumed to be 100Pa and 30°, respectively. It was noted in [53] that shear stress can be computed by assuming either a laminar or turbulent boundary layer, if the roughness of the surface is small compared to the boundary layer thickness. On the other hand, if the roughness is high enough, the shear stress can be estimated by the local dynamic pressure at a distance slightly above the boundary layer. This is the most conservative way to obtain the shear stress, and leads to a much higher value than the shear stress in the laminar/turbulent boundary layer [54].

Weak (one-way) coupling between the dust and carrier gas phases was considered. The simulated particle diameter and particle density were assumed to be 30 $\mu$ m and 3000 kg/m<sup>3</sup>, respectively. The simulations were performed for hover altitudes of 5m and 10m. A schematic of the particle injection based on the erosion rate is illustrated in Fig. 15(b). It is worth noting that the application of the UDF is necessary to simulate the non-uniform mass flow rate that the erosion model provides. The eroded particles were then injected into the flow field as a stream from each surface element.

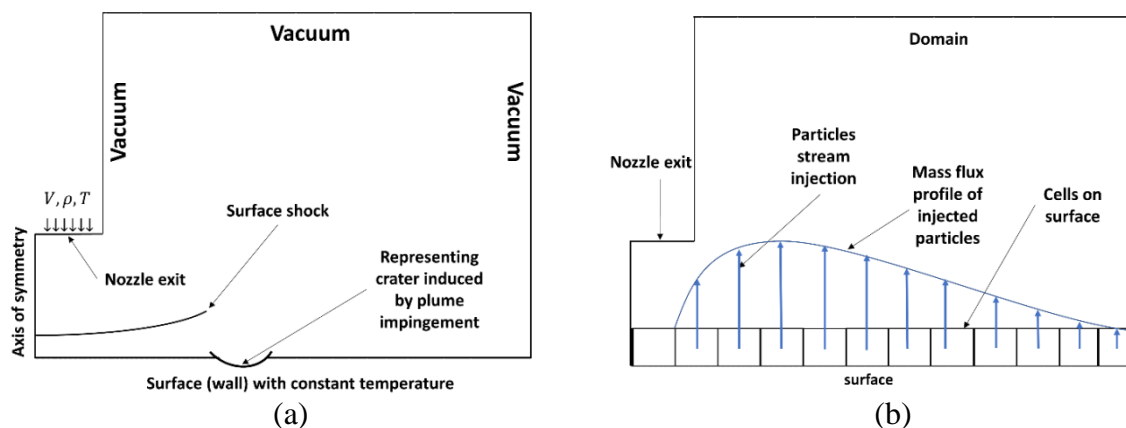


**Fig. 15.** Schematic of a) flow field and b) particle influx from the lunar surface representing eroded particles

A comparison of the computed shear stress and erosion rate with the DSMC solution of Morris *et al.* [53] is illustrated in Fig. 16. The simulation results were found to be in qualitative agreement with each other for both the shear stress and mass flux of particles. As shown in Fig. 16(b), the mass flow rate of the particles increases radially and reaches a maximum after a certain distance (about 2m) from the jet axis where the dynamic pressure is at its peak. The deviation observed in the shear stress is due to the difference in treatment; the local dynamic pressure was calculated at 5cm above the boundary layer in the DSMC solution [53], while it was calculated at 5cm above the surface in the present study, leading to a lower local velocity and dynamic pressure.

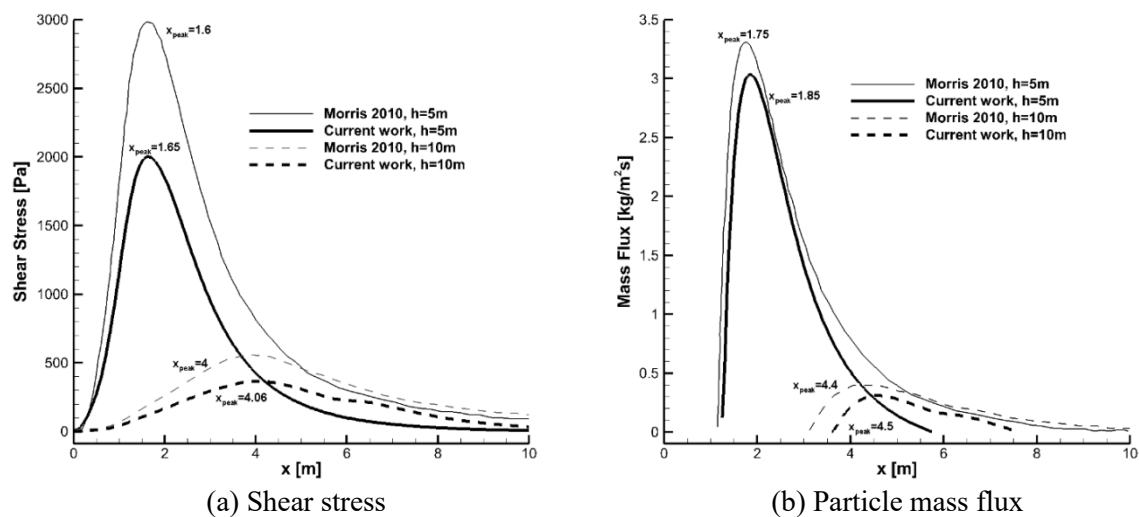


**Fig. 16.** Comparison of erosion modeling parameters with DSMC [53] for different hover altitudes

The streamlines of expanded gas from the nozzle along with the trajectories of eroded particles from the surface are overlaid on the radial gas velocity in Fig. 17. It can be noticed that the motions of grains in the present problem depend largely on the local flow condition. The reason is that, when the velocity equilibration length—the distance required for particle velocity to reach that of the carrier gas—is much smaller than the characteristic length ( $\lambda_p \ll$

L) [55], a particle has enough time to conform to the local carrier phase motion.

Moreover, in Table 3, the maximum particle velocity and the maximum inclined angle of the lofted particles for a hovering altitude of 5m are compared with the DSMC solution [53]. The present results were found to be in qualitative agreement with the DSMC solutions, including the general pattern of trajectories and the inclined angle of eroded particles. Some deviations can be attributed to the different treatment of the local dynamic pressure in the erosion model; 5cm above the boundary layer in the DSMC solutions versus 5cm above the surface in the present study.

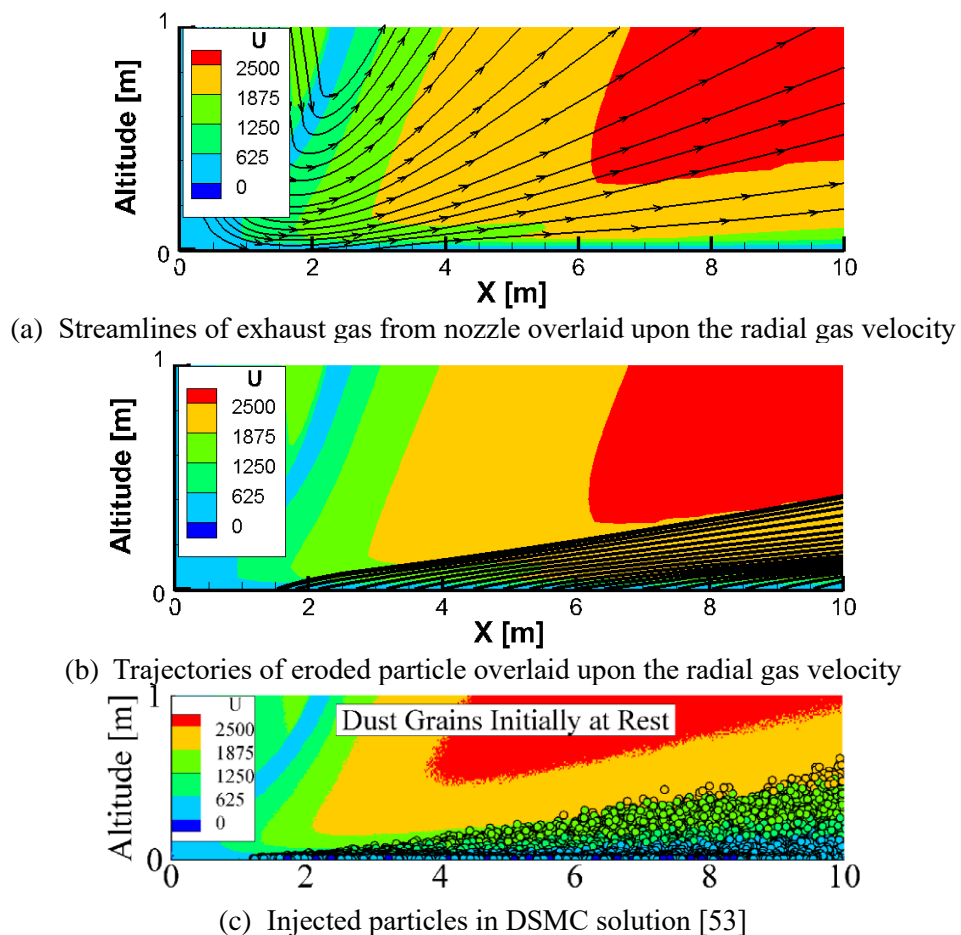
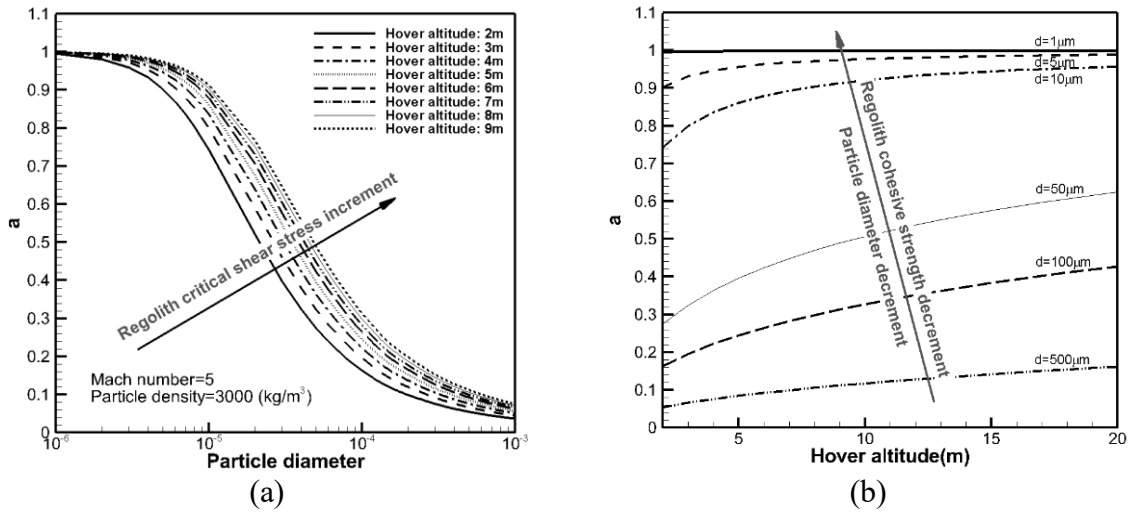


Fig. 17. Dust grains overlaid upon radial velocity ( $D_p = 30\mu m, h = 5m$ )

**Table 3.** Comparison of maximum surface shear stress, maximum particle velocity and maximum particle inclined angle from the surface at a 10m radial distance from the nozzle axis ( $D_p = 30\mu m$ , hover altitude = 5m)

|              | Max. shear stress (Pa) | Max. particle velocity (m/s) | Max. particle inclined angle |
|--------------|------------------------|------------------------------|------------------------------|
| DPLR [53]    | 2995                   | 1700                         | 2.8°                         |
| Present work | 2000                   | 1640                         | 2.0°                         |

To obtain better insight regarding the role of the critical parameter  $a$  in Roberts' theory—the fraction of velocity that the particles gain from the carrier phase—a sensitivity analysis based on the equations (5)-(8) was conducted. In Fig. 18, the parameter  $a$  for a given threshold shear stress is plotted for varying particle diameter, hover altitude, Mach number of flow, and the number density of particles. For very small particle diameters, the value of parameter  $a$  becomes close to one, which implies the velocities for dust and carrier phase are identical. On the other hand, as the diameter of the grains increases, the particles move more slowly than the gas phase due to the larger drag force.



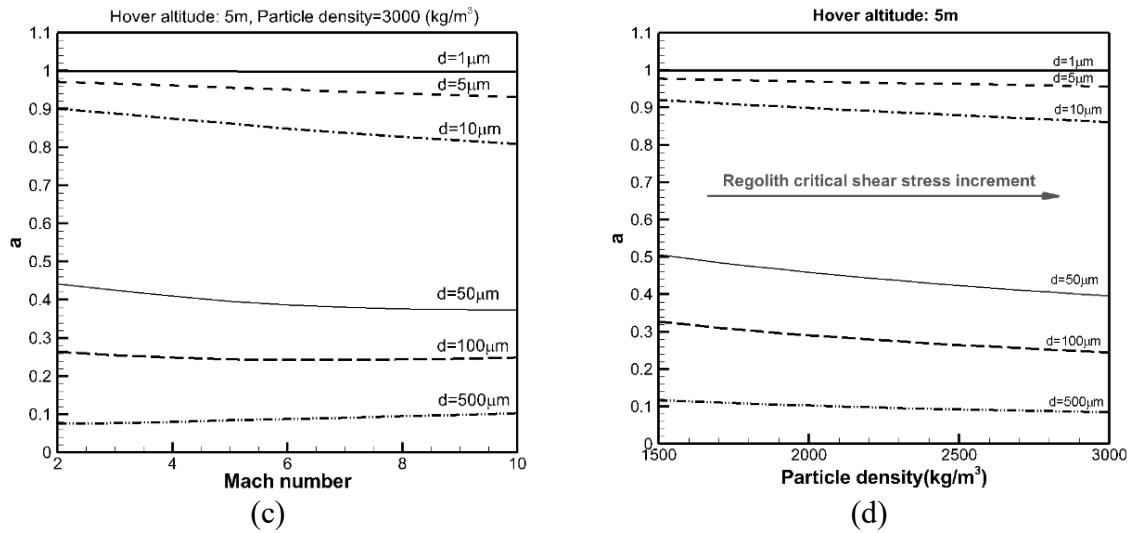


**Fig. 18.** Parametric study on the fraction velocity in the Roberts erosion model

A series of simulations were also conducted to investigate the effect of hover altitude and particle diameter on surface erosion. From Table 4, it can be shown that the maximum particle velocity decreases with increasing particle diameter. This trend remains the same irrespective of hover altitudes and coupling models. Moreover, the maximum velocity of particles in the strongly-coupled two-way case phase is predicted to be lower than that in the loosely-coupled one-way case.

Interestingly, a counter-intuitive trend was found for the maximum inclined angle; the initial decrease was followed by an increase with increasing particle diameter. Apparently, the maximum inclined angle is highly dependent on the Stokes number. When the Stokes number was smaller than 1, the trend decreased, but it increased, when the Stokes number was bigger than 1.

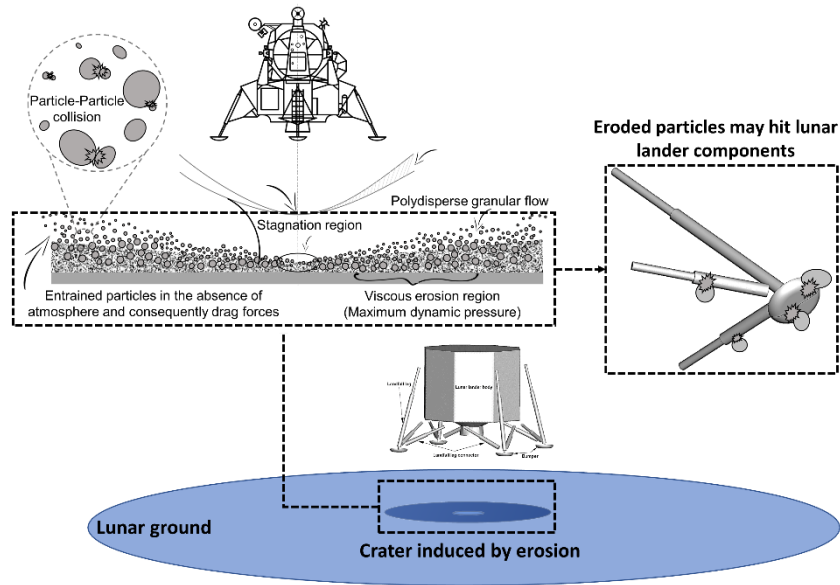
**Table 4.** Comparison of maximum particle velocity and maximum particle inclined angle from the surface at a 10m radial distance from nozzle axis in terms of different hover altitudes and particle diameters

| Hover altitude (m) | Particle diameter ( $\mu m$ ) | Coefficient $\alpha$ | Max. velocity (m/s) |         | Max. inclined angle |         | Stokes number |
|--------------------|-------------------------------|----------------------|---------------------|---------|---------------------|---------|---------------|
|                    |                               |                      | One-way             | Two-way | One-way             | Two-way |               |
| 5                  | 1                             | 0.998                | 2500                | 2390    | 1.4°                | 2.28°   | 0.07577       |
|                    | 10                            | 0.86                 | 2350                | 1460    | 1.2°                | 2.13°   | 0.7577        |
|                    | 30                            | 0.54                 | 1640                | 1050    | 2.0°                | 3.14°   | 2.2732        |
|                    | 50                            | 0.39                 | 1170                | 800     | 2.75°               | 3.86°   | 3.7887        |
| 10                 | 1                             | 0.999                | 1870                | 1720    | 0.47°               | 0.57°   | 0.07577       |
|                    | 10                            | 0.92                 | 1780                | 1625    | 0.41°               | 0.53°   | 0.7577        |
|                    | 30                            | 0.66                 | 1280                | 1170    | 1.02°               | 1.24°   | 2.2732        |
|                    | 50                            | 0.51                 | 930                 | 860     | 1.7°                | 1.93°   | 3.7887        |

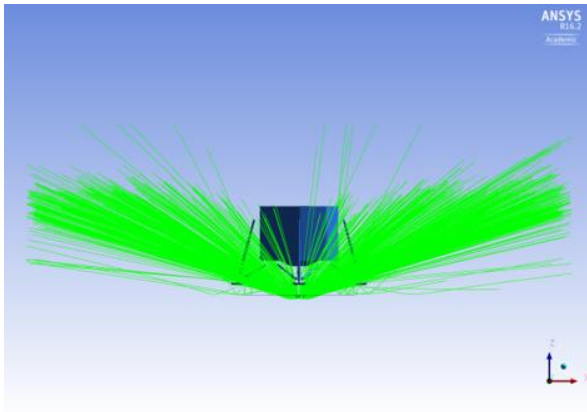
### 5.3 Dispersal simulation of the eroded particles from the induced crater

Small craters can be formed in the lunar surface either by natural processes, like the impact of an object, or by the impingement of the rocket motor plume on the surface. Predicting the trajectories of eroded particles in such circumstances can be useful for the engineering design of a lunar lander. Fig. 19(a) shows a schematic of the lunar lander module hovering above a small crater induced by plume-surface interaction. The crater dimension in the present simulation was chosen based on the experimental results reported in [56].

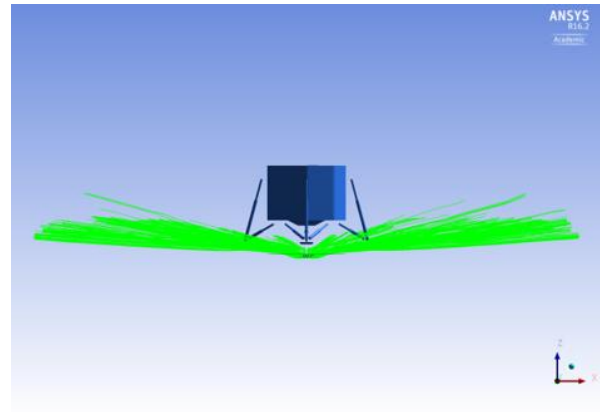
Particles with two different diameters,  $100\mu m$  and  $1\mu m$ , which correspond to  $St=757$  and  $St=0.0757$ , respectively, were injected from the surface. As shown in Fig. 19(b), (d), particles with a high Stokes number move with a higher inclined angle, surrounding the lander module, and with a much higher possibility that the eroded particles will strike the lander components. On the other hand, as shown in Fig. 19(c), (e), particles with a low Stokes number move with a lower inclined angle, so may not strike the module. Consequently, with increasing particle diameter or Stokes number, more careful consideration will be required to protect the module components from particle impact.



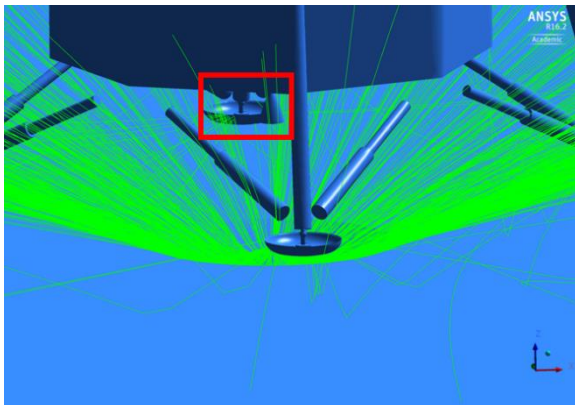
(a) Schematic of the lunar lander module and induced crater



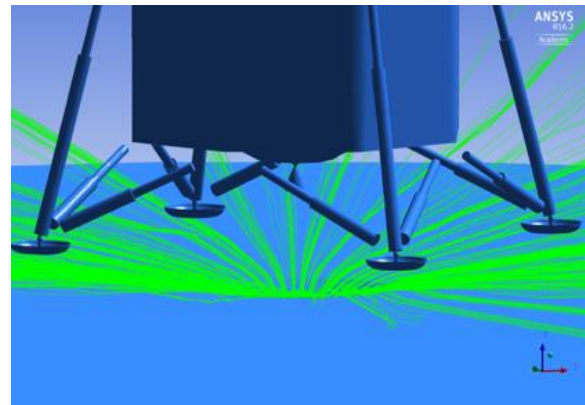
(b) Injected particles with diameter  $100\mu\text{m}$  and  $St = 757$



(c) Injected particles with diameter  $1\mu\text{m}$  and  $St = 0.0757$



(d) Impingement of particles to the bumper ( $100\mu\text{m}$ )



(e) No impingement of particles to the bumper ( $1\mu\text{m}$ )

**Fig. 19.** Particle injection from an induced crater underneath of the jet for particle diameters ( $100\mu\text{m}$ ,  $1\mu\text{m}$ )

## 6. Concluding remarks

The impingement of a rocket plume on the lunar surface can cause significant dust dispersal when the lunar lander approaches a landing site. The present study investigated the near-field plume impingement on the dusty surface of the Moon for a proposed lunar lander configuration, using the physical conservation laws, with first-order NSF constitutive relations in the Eulerian framework for the gas phase, and the particle-based DPM in the Lagrangian framework for the solid phase. The effects of the plume-surface interaction on the lunar lander components were analyzed to provide a more efficient method of obtaining predictive results for engineering design, compared to the computationally expensive DSMC method. In addition, by evaluating a non-equilibrium quantifier and a measure directly related to entropy production in non-equilibrium processes, it was shown that most regions in the near-field interaction of the plume (and in particular, multiple plumes) and the lunar surface at low altitude hover were either in equilibrium or near equilibrium. It is worth mentioning that the expansion of gas into the near-vacuum lunar condition compared to exhaust gas under terrestrial circumstances varies not only in the shape of plume but also in the pressure profile on the surface. The former results in the underexpanded jet, while the latter yields the overexpanded jet.

Simulations of a complicated lunar lander configuration with five nozzles, four bumpers, four landfall legs, and eight connectors were also conducted. The results revealed regions with high pressure and hot spots on the landfall legs, the connectors as well as the bottom of the module, which may impose further design restrictions. To simulate the surface erosion phenomena and consequent entrainment of regolith grains, particles were injected from the surface with an erosion rate calculated using the Roberts' model based on excess shear stress.

The role of the critical parameter in the Roberts' theory—the fraction of velocity that the particles gain from the carrier phase—was investigated for different particle diameters, hover altitude, Mach number of flow, and number density of particles. The flow associated with the eroded particles in the wall jet region resembles the particle-laden flow in an underexpanded jet. The simulation results indicated that the maximum particle velocity decreases with increasing particle diameter, irrespective of hover altitudes and coupling models.

Interestingly, the maximum inclined angle exhibited different behaviors depending on the Stokes number of the flow. For a bed covered with small particles, the corresponding Stokes number is less than 1 and the inclined angle decreased with increasing particle diameter. However, for larger particle diameters with a Stokes number higher than 1, the inclined angle increased with increasing particle diameter.

To investigate the effect of a small crater from which the particles may be entrained into the flow field with a higher inclined angle, a case with the lunar lander hovering above a small crater was simulated. The trajectory of grains revealed that the possibility that eroded particles would strike lander components grew with increasing particle diameter. Hence, extra consideration should be taken to protect module components from particle impact in the presence of a crater with larger size particles.

The present work focused on near-field plume-surface interactions and regolith erosion and dispersal defined by low altitude hover, and the use of a first-order NSF model based on the assumption of not-far-from-equilibrium. However, second-order (or higher) gas kinetic models [57] or DSMC may be necessary to provide a more accurate and far-field description of this multi-physics multi-scale problem. We hope to report the investigation of this challenging problem in future work using second-order Boltzmann-based constitutive relations.

## Nomenclature

|                      |   |                      |  |
|----------------------|---|----------------------|--|
| $a$                  | fraction coefficient                            | $\varphi$            | friction angle                           |
| $C$                  | cohesive stress                                 | $\phi$               | erosion rate                             |
| $C_D$                | drag coefficient                                | $\tau$               | shear stress                             |
| $d$                  | particle diameter                               | $\Pi$                | tensor of shear stress                   |
| $Ec$                 | Eckert number                                   |                      |  |
| $F$                  | additional force                                |                      |  |
| $F_D$                | drag force per unit mass                        | <i>Subscript</i>     |  |
| $F_{th}$             | engine thrust                                   | <i>crit</i>          | critical properties                      |
| $g$                  | gravity acceleration                            | $n$                  | nozzle exit                              |
| $h$                  | hover altitude                                  | $p$                  | particle properties                      |
| $K_h$                | hypersonic factor                               | $r$                  | reference value                          |
| $Kn$                 | Knudsen number                                  | $x$                  | axial coordinate                         |
| $M$                  | Mach number                                     |                      |  |
| $N_\delta$           | degree of non-equilibrium parameter             | <i>Abbreviations</i> |  |
| $P$                  | static pressure                                 | AUSM+                | Advection Upstream Splitting Method Plus |
| $Pr$                 | Prandtl number                                  | BCF                  | Bearing Capacity Failure                 |
| $\mathbf{Q}$         | vector of heat flux                             | DDF                  | Diffusion Driven Flow                    |
| $R$                  | gas constant                                    | DGE                  | Diffused Gas Eruption                    |
| $\hat{R}$            | factor of deviation from near-local-equilibrium | DPLR                 | Data-Parallel Line Relaxations           |
| $Re$                 | Reynolds number                                 | DPM                  | Discrete Phase Model                     |
| $St$                 | Stokes number                                   | DSMC                 | Direct Simulation Monte Carlo            |
| $T$                  | temperature                                     | ESM                  | European Service Module                  |
| $u$                  | velocity  | FVM                  | Finite Volume Method                     |
|                      |   | NSF                  | Navier-Stokes-Fourier                    |
| <i>Greek letters</i> |   | OMS-E                | Orbital Maneuvering System Engine        |
| $\rho$               | mass density                                    | RCS                  | Reaction Control System                  |
| $\mu$                | molecular viscosity                             | UDF                  | User Defined Function                    |
| $\gamma$             | ratio of specific heats                         | VE                   | Viscous Erosion                          |

## Acknowledgments

This work was supported by the National Research Foundation of Korea funded by the Ministry of Science and ICT (NRF 2015-M1A3A3A02-010621, 2017-R1A2B2007634), South Korea. The second author (O.E.) acknowledges the support provided by the institutional research program (K19L03C06) of the Korea Institute of Science and Technology Information (KISTI), South Korea.

## References

- [1] B. Lyndon, Apollo program summary report, Johnson Space Center, NASA, TM X, 68725 (1975).

- [2] I. Klotz, New moon, *Aviation Week & Space Technology* November 27-December 10 (2017) 60-61.
- [3] K.H. Lee, Lunar orbiter trade study and conceptual design of onboard propulsion system, *Journal of Spacecraft and Rockets* 48 (2011) 346-354.
- [4] Apollo 16 Astronaut John Young, (July 2004).
- [5] A. Tosh, P.A. Liever, R.R. Arslanbekov, S.D. Habchi, Numerical analysis of spacecraft rocket plume impingement under lunar environment, *Journal of Spacecraft and Rockets* 48 (2011) 93.
- [6] J.A. Morfiño, J.J. Salvá, Numerical study of the start-up process in an optimized rocket nozzle, *Aerospace Science and Technology* 12 (2008) 485-489.
- [7] A. Hadjadj, Y. Perrot, S. Verma, Numerical study of shock/boundary layer interaction in supersonic overexpanded nozzles, *Aerospace Science and Technology* 42 (2015) 158-168.
- [8] G. Hagemann, M. Frey, Shock pattern in the plume of rocket nozzles: needs for design consideration, *Shock Waves* 17 (2008) 387-395.
- [9] I.E. Wrisdale, D.F. Mikulskis, M.R. Gilmore, Navier-Stokes calculations of a twin-nozzle rocket plume, *AIAA Paper* (1996).
- [10] H.B. Ebrahimi, J. Levine, A. Kawasaki, Numerical investigation of twin-nozzle rocket plume phenomenology, *Journal of Propulsion and Power* 16 (2000) 178-186.
- [11] H.B. Ebrahimi, Numerical investigation of multi-plume rocket phenomenology, 33<sup>rd</sup> Joint Propulsion Conference and Exhibit (1997) 2942.
- [12] C.C. Kiris, J.A. Housman, M.F. Barad, C. Brehm, E. Sozer, S. Moini-Yekta, Computational framework for launch, ascent, and vehicle aerodynamics (LAVA), *Aerospace Science and Technology* 55 (2016) 189-219.
- [13] R.F. Scott, H.-Y. Ko, Transient rocket-engine gas flow in soil, *AIAA Journal* 6 (1968) 258-264.
- [14] X. He, B. He, G. Cai, Simulation of rocket plume and lunar dust using DSMC method, *Acta Astronautica* 70 (2012) 100-111.
- [15] A.B. Morris, D.B. Goldstein, P.L. Varghese, L.M. Trafton, Approach for modeling rocket plume impingement and dust dispersal on the moon, *Journal of Spacecraft and Rockets* 52 (2015) 362-374.
- [16] K. Khasawneh, H. Liu, C. Cai, Highly rarefied two-dimensional jet impingement on a flat plate, *Physics of Fluids* 22 (2010) 117101.
- [17] C. Cai, X. Huang, High-speed rarefied round jet and jet impingement flows, *AIAA Journal* 50 (2012) 2908-2918.
- [18] S. Cai, C. Cai, K. Zhang, J. Li, Rarefaction effects on jet impingement loads, *Aerospace* 4 (2017) 48.
- [19] B. He, X. He, M. Zhang, G. Cai, Plume aerodynamic effects of cushion engine in lunar landing, *Chinese Journal of Aeronautics* 26 (2013) 269-278.
- [20] J.T. Yim, F. Sibé, N. Jerardo, Plume impingement analysis for the european service module propulsion system, 50th AIAA/ASME/SAE/ASEE Joint Propulsion Conference (2014) 3883.
- [21] D.K.A. A. Sharma, J. C. Pisharady, S. Sunil Kumar, Plume Flow Field Analysis for Lander Propulsion System of Chandrayaan-2 Mission, 68th International Astronautical Congress (IAC) (2017) 11.
- [22] G. Zheng, H. Nie, J. Chen, C. Chen, H.P. Lee, Dynamic analysis of lunar lander during soft landing using explicit finite element method, *Acta Astronautica* 148 (2018) 69-81.
- [23] X. Wei, Q. Lin, H. Nie, M. Zhang, J. Ren, Investigation on soft-landing dynamics of four-legged lunar lander, *Acta Astronautica* 101 (2014) 55-66.
- [24] S. Singh, A. Karchani, R.S. Myong, Non-equilibrium effects of diatomic and polyatomic gases on the shock-vortex interaction based on the second-order constitutive model of the Boltzmann-Curtiss equation, *Physics of Fluids* 30 (2018) 016109.
- [25] N. Le, H. Xiao, R.S. Myong, A triangular discontinuous Galerkin method for non-Newtonian implicit constitutive models of rarefied and microscale gases, *Journal of Computational Physics* 273 (2014) 160-184.
- [26] R.S. Myong, A generalized hydrodynamic computational model for rarefied and microscale diatomic gas flows, *Journal of Computational Physics* 195 (2004) 655-676.
- [27] R.S. Myong, A computational method for Eu's generalized hydrodynamic equations of rarefied and microscale gasdynamics, *Journal of Computational Physics* 168 (2001) 47-72.
- [28] R.S. Myong, Thermodynamically consistent hydrodynamic computational models for high-Knudsen-number gas flows, *Physics of Fluids* 11 (1999) 2788-2802.
- [29] M. Gallis, J. Torczynski, D. Rader, An approach for simulating the transport of spherical particles in a rarefied gas flow via the direct simulation Monte Carlo method, *Physics of Fluids* 13 (2001) 3482-3492.
- [30] J. Burt, I. Boyd, Development of a two-way coupled model for two phase rarefied flows, 42nd AIAA Aerospace Sciences Meeting and Exhibit, 2004, pp. 1351.
- [31] L. Roberts, The interaction of a rocket exhaust with the lunar surface, *The Fluid Dynamic Aspects of Space Flight*, Proceeding of the AGARD-NATO Specialists Meeting, 1966, pp. 269-290.

- [32] L. Roberts, J. South, Comments on exhaust flow field and surface impingement, *AIAA Journal* 2 (1964) 971-973.
- [33] J.E. Lane, P.T. Metzger, C.D. Immer, X. Li, Lagrangian trajectory modeling of lunar dust particles, *Earth & Space 2008: Engineering, Science, Construction, and Operations in Challenging Environments* (2008) 1-9.
- [34] J.E. Lane, P.T. Metzger, J. Carlson, Lunar dust particles blown by lander engine exhaust in rarefied and compressible flow, *Earth and Space 2010: Engineering, Science, Construction, and Operations in Challenging Environments* (2010) 134-142.
- [35] Y. Li, D. Ren, Z. Bo, W. Huang, Q. Ye, Y. Cui, Gas-particle two-way coupled method for simulating the interaction between a rocket plume and lunar dust, *Acta Astronautica* (2018).
- [36] O. Ejtehadi, A. Rahimi, A. Karchani, R.S. Myong, Complex wave patterns in dilute gas-particle flows based on a novel discontinuous Galerkin scheme, *International Journal of Multiphase Flow* 104 (2018) 125-151.
- [37] J.D. Schwarzkopf, M. Sommerfeld, C.T. Crowe, Y. Tsuji, *Multiphase Flows with Droplets and Particles*, CRC Press (2011).
- [38] P.T. Metzger, J.E. Lane, C.D. Immer, Modification of Roberts' theory for rocket exhaust plumes eroding lunar soil, *Earth & Space 2008: Engineering, Science, Construction, and Operations in Challenging Environments* (2008) 1-8.
- [39] R.J. LeVeque, *Finite Volume Methods for Hyperbolic Problems*, Cambridge University Press (2002).
- [40] M.S. Liou, A sequel to AUSM, Part II: AUSM+<sup>up</sup> for all speeds, *Journal of Computational Physics* 214 (2006) 137-170.
- [41] ANSYS FLUENT User Manuals V14.0 ANSYS, Inc. (2012).
- [42] ANSYS FLUENT Theory Guide Knowl. Creat. Diffus. Util 15317 (2011) 724-746.
- [43] S. Morsi, A. Alexander, An investigation of particle trajectories in two-phase flow systems, *Journal of Fluid Mechanics* 55 (1972) 193-208.
- [44] P.T. Metzger, J. Smith, J.E. Lane, Phenomenology of soil erosion due to rocket exhaust on the Moon and the Mauna Kea lunar test site, *Journal of Geophysical Research: Planets* 116 (2011).
- [45] Y. Shao, *Physics and Modelling of Wind Erosion*, Springer Science & Business Media (2008).
- [46] A.B. Morris, *Simulation of Rocket Plume Impingement and Dust Dispersal on the Lunar Surface*, Ph.D. Dissertation (2012).
- [47] H.S. Tsien, Superaerodynamics, mechanics of rarefied gases, *Journal of the Aeronautical Sciences* 13 (1946) 653-664.
- [48] R.S. Myong, Gaseous slip models based on the Langmuir adsorption isotherm, *Physics of Fluids* 16 (2004) 104-117.
- [49] M. Sommerfeld, The structure of particle-laden, underexpanded free jets, *Shock Waves* 3 (1994) 299-311.
- [50] J.D. Anderson, *Modern Compressible Flow: with Historical Perspective*, McGraw-Hill New York (1990).
- [51] M. Mehta, A. Sengupta, N.O. Renno, J.W.V. Norman, P.G. Huseman, D.S. Gulick, M. Pokora, Thruster plume surface interactions: Applications for spacecraft landings on planetary bodies, *AIAA Journal* 51 (2013) 2800-2818.
- [52] O. Ejtehadi, A. Rahimi, R.S. Myong, Numerical investigation of the counter-intuitive behavior of Mach disc movement in underexpanded gas-particle jets, *Journal of Computational Fluids Engineering* 24 (2019) 19-28.
- [53] A. Morris, D. Goldstein, P. Varghese, L. Trafton, Plume impingement on a dusty lunar surface, *AIP Conference Proceedings* (2011) 1187-1192.
- [54] L. Roberts, The action of a hypersonic jet on a dust layer, *IAS Paper No. 65-50*, Institute of the Aerospace Sciences 31st Annual Meeting (1963) 21-23.
- [55] F.E. Marble, Dynamics of a gas containing small solid particles, *Combustion and Propulsion* (1963) 175-213.
- [56] N.S. Land, L.V. Clark, Experimental investigation of jet impingement on surfaces of fine particles in a vacuum environment, *National Aeronautics and Space Administration*, 2633 (1965).
- [57] O. Ejtehadi, R.S. Myong, A modal discontinuous Galerkin method for simulating dusty and granular gas flows in thermal non-equilibrium in the Eulerian framework, *Journal of Computational Physics* 411 (2020) 109410.